Research Paper

GEOSPHERE

GEOSPHERE, v. 16

https://doi.org/10.1130/GES02263.1

11 figures; 1 table; 1 supplemental file

CORRESPONDENCE: ahatem@usgs.gov

CITATION: Hatem, A.E., Dolan, J.F., Zinke, R.W., Langridge, R.M., McGuire, C.P., Rhodes, E.J., Brown, N., and Van Dissen, R.J., 2020, Holocene to latest Pleistocene incremental slip rates from the east-central Hope fault (Conway segment) at Hossack Station, Marlborough fault system, South Island, New Zealand: Towards a dated path of earthquake slip along a plate boundary fault: Geosphere, v. 16, https://doi.org/10.1130/GES02263.1.

Science Editor: Andrea Hampel
Associate Editor: Andrew V. Zuza

Received 31 March 2020
Revision received 17 July 2020
Accepted 1 September 2020

Holocene to latest Pleistocene incremental slip rates from the east-central Hope fault (Conway segment) at Hossack Station, Marlborough fault system, South Island, New Zealand: Towards a dated path of earthquake slip along a plate boundary fault

Alexandra E. Hatem[1,*], James F. Dolan[1], Robert W. Zinke[1,†], Robert M. Langridge[2], Christopher P. McGuire[3,§], Edward J. Rhodes[3,4], Nathan Brown[3,#], and Russell J. Van Dissen[2]

[1]Department of Earth Sciences, University of Southern California, 3651 Trousdale Parkway, Los Angeles, California 90089, USA
[2]GNS Science–Lower Hutt, 1 Fairway Drive, Avalon, Lower Hutt 5011, New Zealand
[3]Department of Earth, Planetary, and Space Sciences, University of California, Los Angeles, 595 Charles E Young Drive East, Los Angeles, California 90095, USA
[4]Department of Geography, University of Sheffield, Western Bank, Sheffield S10 2TN, UK

ABSTRACT

Geomorphic field and aerial lidar mapping, coupled with fault-parallel trenching, reveals four progressive offsets of a stream channel and an older offset of the channel headwaters and associated fill terrace–bedrock contact at Hossack Station along the Conway segment of the Hope fault, the fastest-slipping fault within the Marlborough fault system in northern South Island, New Zealand. Radiocarbon and luminescence dating of aggradational surface deposition and channel initiation and abandonment event horizons yields not only an average dextral rate of ~15 mm/yr since ca. 14 ka, but also incremental slip rates for five different time periods (spanning hundreds to thousands of years) during Holocene to latest Pleistocene time. These incremental rates vary through time and are, from youngest to oldest: 8.2 +2.7/–1.5 mm/yr averaged since 1.1 ka; 32.7 +~124.9/–10.1 mm/yr averaged over 1.61–1.0 ka; 19.1 ± 0.8 mm/yr between 5.4 and 1.6 ka; 12.0 ± 0.9 mm/yr between 9.4 and 5.4 ka, and 13.7 +4.0/–3.4 mm/yr from 13.8 to 9.4 ka, with generally faster rates in the mid- to late Holocene relative to slower rates prior to ca. 5.4 ka. The most pronounced variation in rates occurs between the two youngest intervals, which are averaged over shorter time spans (≤1700 yr) than the three older incremental rates (3700–4500 yr). This suggests that the factor of ~1.5× variations in Hope fault slip rate observed in the three older, longer-duration incremental rates may mask even greater temporal variations in rate over shorter time scales.

INTRODUCTION

Understanding the rate at which faults store and release elastic strain energy is of fundamental importance for a wide range of issues, from seismic hazard assessment to informed interpretation of geodetic data to the strength and evolution of faults. Previous analyses of incremental fault slip rates indicate a wide range of behaviors, from rates that are seemingly constant over a wide range of time scales (e.g., Weldon and Sieh, 1985; Noriega et al., 2006; Kozaci et al., 2007; Gold and Cowgill, 2011; Van Der Woerd et al., 2002; Salisbury et al., 2018) to examples in which strain release is markedly nonconstant (e.g., Friedrich et al., 2003; Weldon et al., 2004; Mason et al., 2006; Gold and Cowgill, 2011; Onderdonk et al., 2015; Dolan et al., 2016; Zinke et al., 2017, 2019). Despite a growing number of studies, the overall dearth of these slip-rate data from major faults globally hampers our ability to understand the causes of such behavior. In this study, we document incremental slip rates over five different Holocene to latest Pleistocene time intervals on the Hope fault, one of the fastest-slipping strike-slip faults in the Australian-Pacific plate boundary in northern South Island, New Zealand (e.g., Litchfield et al., 2014). We discuss these results in light of their implications for plate-boundary strain accommodation, fault mechanics, and potential use in probabilistic seismic hazard analysis.

The Marlborough Fault System and Hope Fault

The Pacific-Australian plate boundary cuts across the South Island of New Zealand, which spans the onshore gap between subduction zones of opposing polarity, with the Hikurangi megathrust dipping northwest off the east coast of North Island and the Puysegar megathrust dipping southeast off the southwestern coast of southern South Island (Fig. 1A). In northern South Island, most relative plate motion is accommodated by the Marlborough fault system, a system of subparallel right-lateral strike-slip faults that splay northeastward from the Alpine fault, the main plate-boundary fault to the

Alexandra E. Hatem https://orcid.org/0000-0001-7584-2235
*Now at Geologic Hazards Science Center, U.S. Geological Survey, 1711 Illinois Street, Golden, Colorado 80401, USA
†Now at Jet Propulsion Laboratory, 4732 Oak Grove Drive, La Cañada Flintridge, California 91011, USA
§Now at Grant Institute, University of Edinburgh, The King's Buildings, James Hutton Road, Edinburgh EH9 3FE, UK
#Now at Department of Earth and Planetary Science, University of California, Berkeley, 307 McCone Hall, Berkeley, California 94720-4767, USA

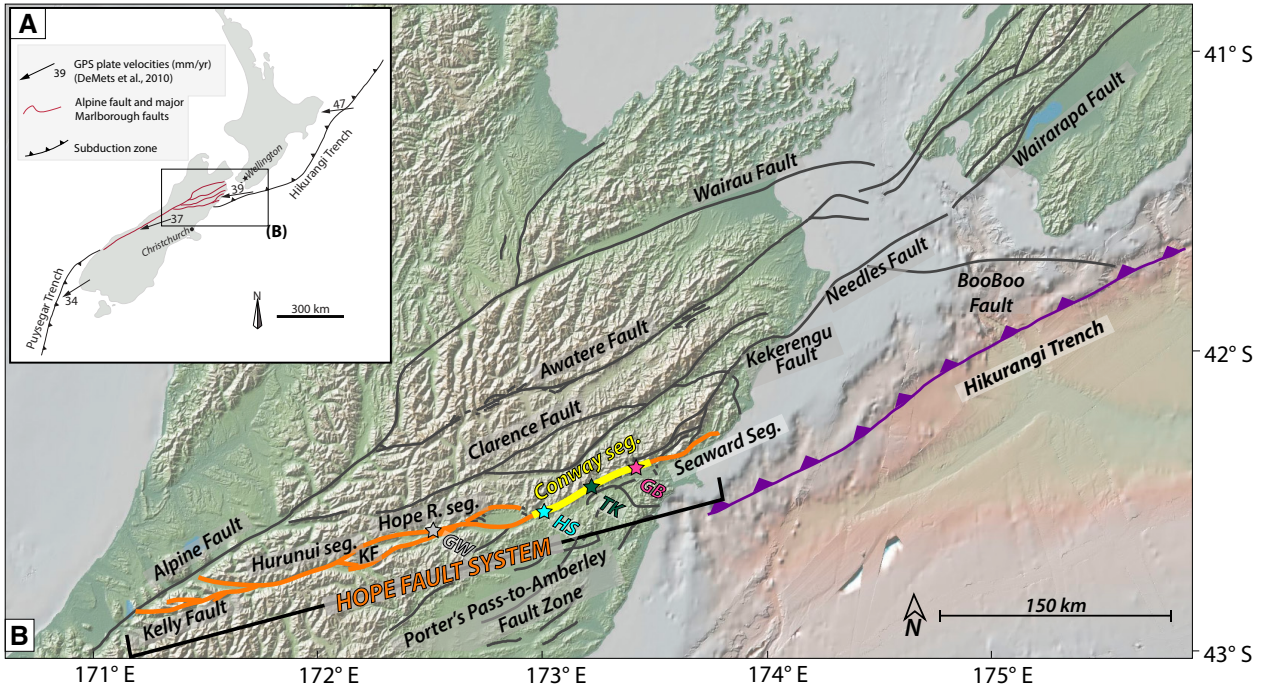

Figure 1. (A) Map of New Zealand with relative plate motion vectors (DeMets et al., 2010). Red lines delineate the Alpine fault and major faults within the Marlborough fault network within the northern South Island. (B) Regional fault map showing the Alpine fault, Marlborough fault system, and major North Island faults. The Hope fault system is shown in orange and yellow. The on-land Hope fault system includes, from west to east, the Kelly fault, Hurunui segment, Hope River segment, Conway segment, and Seaward segment; the Conway segment is shown in yellow. Blue star denotes the Hossack Station study site (HS) (this study); green star denotes the Terako single-event displacement site (TK) (Beauprêtre et al., 2012); pink star denotes the Green Burn paleoearthquake site (GB) (Hatem et al., 2019). KF—Kakapo fault; GW—Glynne Wye. Fault map is adapted from Langridge et al. (2016).

southwest (Fig. 1B). From north to south, the four main faults of the Marlborough fault system, which collectively accommodate ~80%–90% of the total plate motion of ~39 mm/yr (DeMets et al., 2010; Wallace et al., 2012; Litchfield et al., 2014), are the Wairau, Awatere, Clarence, and Hope faults. Within the Marlborough fault system, the southernmost Hope fault is thought to have the fastest slip rate, estimated by previous workers to exceed 10 mm/yr along the majority of its on-land length (Cowan, 1990; Cowan and McGlone, 1991; Langridge and Berrymxan, 2005; Langridge et al., 2016; Khajavi et al., 2018). Along the single-stranded, east-central part of the fault, the slip rate has been estimated to be as fast as ~20–25 mm/yr over mid-Holocene time scales (McMorran, 1991; Van Dissen and Yeats, 1991; Langridge et al., 2003). Previous work shows that the Holocene–late Pleistocene slip rate of the Hope fault may have varied through time. Utilizing weathering-rind age estimates, Knuepfer (1992) suggested that slip rate along the Hope fault may have varied by as much as an order of magnitude over millennial time scales. More recently, to the west of our study area, where slip is partitioned between the Hope fault and southern Kakapo strand, Khajavi et al. (2018) documented similar variations in slip rate during Holocene time on the northern Hope fault strand.

The focus of this study is the Conway segment of the Hope fault. The Conway segment is a structural segment on the east-central part of the Hope fault bounded at its southwestern end by the ~7-km-wide transtensional Hanmer Basin (Wood et al., 1994) and at its northeastern end by a structurally complex transition in which most slip is thought to be transferred northeastward from the Hope fault onto the fast-slipping oblique-reverse faults of the Jordan-Kekerengu fault system (Van Dissen and Yeats, 1991; Van Dissen et al., 2016; Kearse et al., 2017) (Fig. 1B). The Conway segment has not generated a surface-rupturing earthquake since the arrival of European settlers in this part of New Zealand ca. 1840 CE. Although minor ground deformation was observed at an isolated location ~40 km east of the Hossack Station study site following the 2016 CE M_w

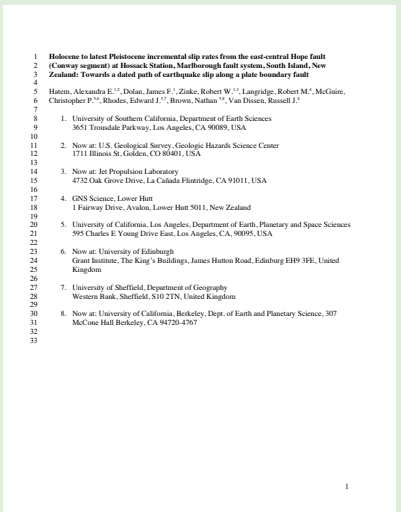

Holocene to latest Pleistocene incremental slip rates from the east-central Hope fault (Conway segment) at Hossack Station, Marlborough fault system, South Island, New Zealand: Towards a dated path of earthquake slip along a plate boundary fault

Hatem, Alexandra E.[1,2], Dolan, James F.[1], Zinke, Robert W.[1,3], Langridge, Robert M.[4], McGuire, Christopher P.[5,6], Rhodes, Edward J.[7,8], Brown, Nathan[7,9], Van Dissen, Russell J.[4]

1. University of Southern California, Department of Earth Sciences 3651 Trousdale Parkway, Los Angeles, CA 90089, USA
2. Now at: U.S. Geological Survey, Geologic Hazards Science Center 1711 Illinois St, Golden, CO 80401, USA
3. Now at: Jet Propulsion Laboratory 4732 Oak Grove Drive, La Cañada Flintridge, CA 91011, USA
4. GNS Science, Lower Hutt 1 Fairway Drive, Avalon, Lower Hutt 5011, New Zealand
5. University of California, Los Angeles, Department of Earth, Planetary and Space Sciences 595 Charles E Young Drive East, Los Angeles, CA, 90095, USA
6. Now at: University of Edinburgh Grant Institute, The King's Buildings, James Hutton Road, Edinburg EH9 3FE, United Kingdom
7. University of Sheffield, Department of Geography Western Bank, Sheffield, S10 2TN, United Kingdom
8. Now at: University of California, Berkeley, Dept. of Earth and Planetary Science, 307 McCone Hall Berkeley, CA 94720-4767

7.8 Kaikōura earthquake, the majority of the Conway segment did not exhibit any signs of surface rupture (Litchfield et al., 2018; Hatem et al., 2019). In contrast to the Conway segment, the Hurunui and Hope River segments of the Hope fault immediately west of the Hanmer Basin ruptured together in the 1888 CE M_w ~7.1–7.3 Amuri earthquake (McKay, 1890; Cowan, 1990, 1991; Cowan and McGlone, 1991; Khajavi et al., 2016).

Hossack Station Study Site

The study site is located on Hossack Station along the western part of the Conway segment, ~3 km east of the eastern end of the Hanmer Basin (Figs. 1B, 2A–2E). At the study site, the Hope fault is single stranded and strikes ~075°, extending across a broad valley filled by an aggradational fluvial deposit, which is capped by a planar, gently west-dipping terrace tread that we refer to as surface S1. Surface S1 is similar to other valley-filling fluvial gravel terraces that characterize many large river systems in northern South Island that have been dated at ca. 12–15 ka (Khajavi et al., 2016; Zinke et al., 2017, 2019). These ages support earlier depositional models suggesting that extensive fill terraces were deposited at the end of the Last Glacial Maximum when large sediment loads exceeded stream capacity, leading to widespread aggradation (Lensen, 1968; Bull and Knuepfer, 1987; Bull, 1991, 2008).

At the Hossack Station study site, surface S1 has been incised by channels flowing westward to the Hanmer River (Figs. 2A, 2B, 2D). One prominent stream that extends along the southern margin of the valley has looped back and forth across the Hope fault, yielding the progressive stream offsets that are the focus of this study. The site was previously identified by Freund (1971) and studied by McMorran (1991), who both noted progressive offsets of this channel. Based on previous observations, we refer to this stream as the "Loops Stream." McMorran (1991) used observations in trenches, pits, and auger borehole transects, together with radiocarbon dating, to document a late Holocene (ca. 3.6 ka) slip rate of 18 ± 8 mm/yr.

We identify four progressive fault offsets of the Loops Stream at the Hossack Station site, as well as an older offset of the headwaters of Loops Stream and adjacent topography <1 km east of the main study site (Figs. 2B, 2C; –42.538387°, 172.973001°). These progressive Hope fault offsets are documented here using detailed geomorphic mapping both in the field and through analysis of aerial photos and the high-resolution (>12 points/m^2) lidar data that we collected in 2014 (https://doi.org/10.5069/G9G44N75 available at www.opentopography.org). We refer to these progressive offsets as offset A (youngest) to offset E (oldest).

To the south of the fault, the active Loops Stream course flows through a channel that has been incised by ~5 m into the S1 surface, with steep to near-vertical channel walls. The active stream (which we refer to as channel C1) locally flows northward nearly perpendicular to the fault and makes an abrupt, near-90° turn to the west where it meets, and flows westward along, the Hope fault (Figs. 2D, 2E). The sharply defined right-lateral offset of the incised channel wall on the outside of this 90° bend provides the youngest offset we identify (offset A; Fig. 3). An older alignment of the deeply incised channel C1 defines offset B (Fig. 3). Two still-older, now-abandoned, less-incised stream channel courses (channel C2 [older than C1] and channel C3 [older than C2]) provide longer-term estimates for fault offset of the Loops Stream (offsets C and D, respectively; Fig. 3). We describe each of these four Loops Stream offsets in detail below, from oldest to youngest. We follow these descriptions with documentation of the oldest offset we observe at the Hossack Station site, which is defined by restoration of the Loops Stream headwaters and the displaced contact between the surface S1 fill-terrace fluvial gravels and the bedrock canyon walls against which they form a buttress unconformity. We refer to this oldest restoration as offset E (Fig. 2B).

To better define the geometric relationships between paleochannel morphology and the local Hope fault orientation, and to collect samples for radiocarbon and luminescence dating to constrain the ages of the offset channels C1–C3 as well as surface S1, we excavated three fault-parallel trenches and seven sample pits. We dated a total of 62 radiocarbon samples and eight post-infrared (post-IR) infrared stimulated luminescence (IRSL; Supplemental Material[1]) samples from these excavations. Radiocarbon samples, including detrital charcoal, wood, seeds, and other plant matter, were prepared using standard acid-base-acid pretreatment and analyzed at the University of California, Irvine, W.M. Keck accelerator mass spectrometer facility. Radiocarbon age results were then calibrated to calendric years using the most up-to-date Southern Hemisphere calibration curve, SHCal13 (Hogg et al., 2013), using the program OxCal (Bronk Ramsey, 2009). Luminescence samples were prepared and analyzed at the University of California, Los Angeles, using the newly developed post-IR-$IRSL_{225}$ single-grain method (Rhodes, 2015; Lewis et al., 2017; Zinke et al., 2017; see Supplemental Material for explanation of method). All age data were modeled using Bayesian statistics in OxCal. All radiocarbon and luminescence ages mentioned in the text and shown on the figures are in units of years before the year 2019 CE, with the exception of the oldest luminescence ages, which are listed in units of thousands of years ago (ka).

In the following, our documentation of each of these five Loops Stream progressive offsets includes sections describing (1) the geomorphology and geometry of past streamflow, (2) age control on these different configurations of the Loops Stream, and (3) constraints on measurements of the fault offset. The reported uncertainties in sample ages are 2σ, as calculated using the program OxCal (Bronk Ramsey, 2009), and the reported uncertainties in offset determination are based on sedimentological and structural limits on possible streamflow geometries. We follow these descriptions with a detailed summary of all of our observations, synthesizing the data from all five offsets.

GEOMORPHIC, STRATIGRAPHIC, AND CHRONOLOGIC OBSERVATIONS OF OFFSET LOOPS STREAM CHANNELS

We begin by describing the four closely spaced stream offsets at the main (western) study site and follow with a description of the older offset of

[1]Supplemental Material. Includes IRSL detailed procedures with figures and a table, line log of trench 3, and an alternative restoration of offset B. Please visit https://doi.org/10.1130/GEOS.S.12904466 to access the supplemental material, and contact editing@geosociety.org with any questions.

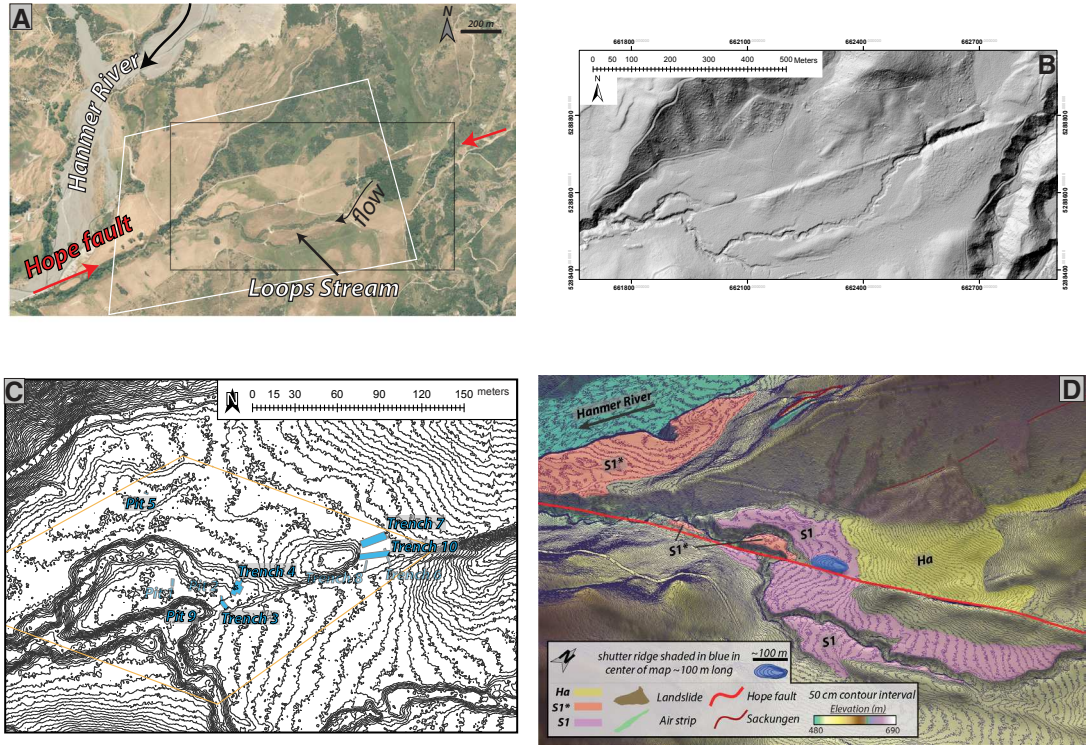

Figure 2. (A) Satellite image of the Hossack Station study site (imagery from ESRI). The Hope fault is indicated with red arrows. Loops Stream and Hanmer River are indicated with black arrows, including flow direction. Black box is the region shown in panel B; white box is the region of the oblique view in panel D. (B) Shaded-relief image of lidar-derived topography at the Hossack Station site. Region of restoration of offset E is labeled. Field of view is the black rectangle in panel A. White box is the region shown in panel C. (C) Topographic map at nadir of the area outlined in panel B. Contour interval is 50 cm. Trenches and pits discussed in this manuscript are shown in blue; trenches not discussed herein are shown in gray. Yellow outline shows the area of panel E. Shutter ridge is shown in blue shading. (D) Oblique view, looking northwest, of the topography of the area outlined in white in panel A. A prominent valley-filling surface is shown in purple (S1); a similar, relatively flat surface S1* is shown in pink, but S1* is at a slightly lower elevation (<2 m) than S1. Shutter ridge is shown in blue shading. Contour interval is 50 cm. Background is a shaded-relief digital elevation model. Topographic data used in this figure are from lidar dataset available referenced in manuscript. (E) Oblique view, looking northwest, of the topography in the area outlined in yellow in panel C. Channels C1–C3 are shown in decreasing saturations of gray overlay. Offset restoration areas are labeled. Trench and pit locations are gray polygons. Contour interval is 50 cm. Background color is a shaded-relief digital elevation model. Topographic data used in this figure are from lidar dataset available referenced in manuscript. Shutter ridge (highlighted in blue in panels C and D) is located between the downstream extents of C2 and C3. Graticule at map edges are in reference frame NZGD2000. Center of field of view in each panel ~–42.538057°, 172.974219°.

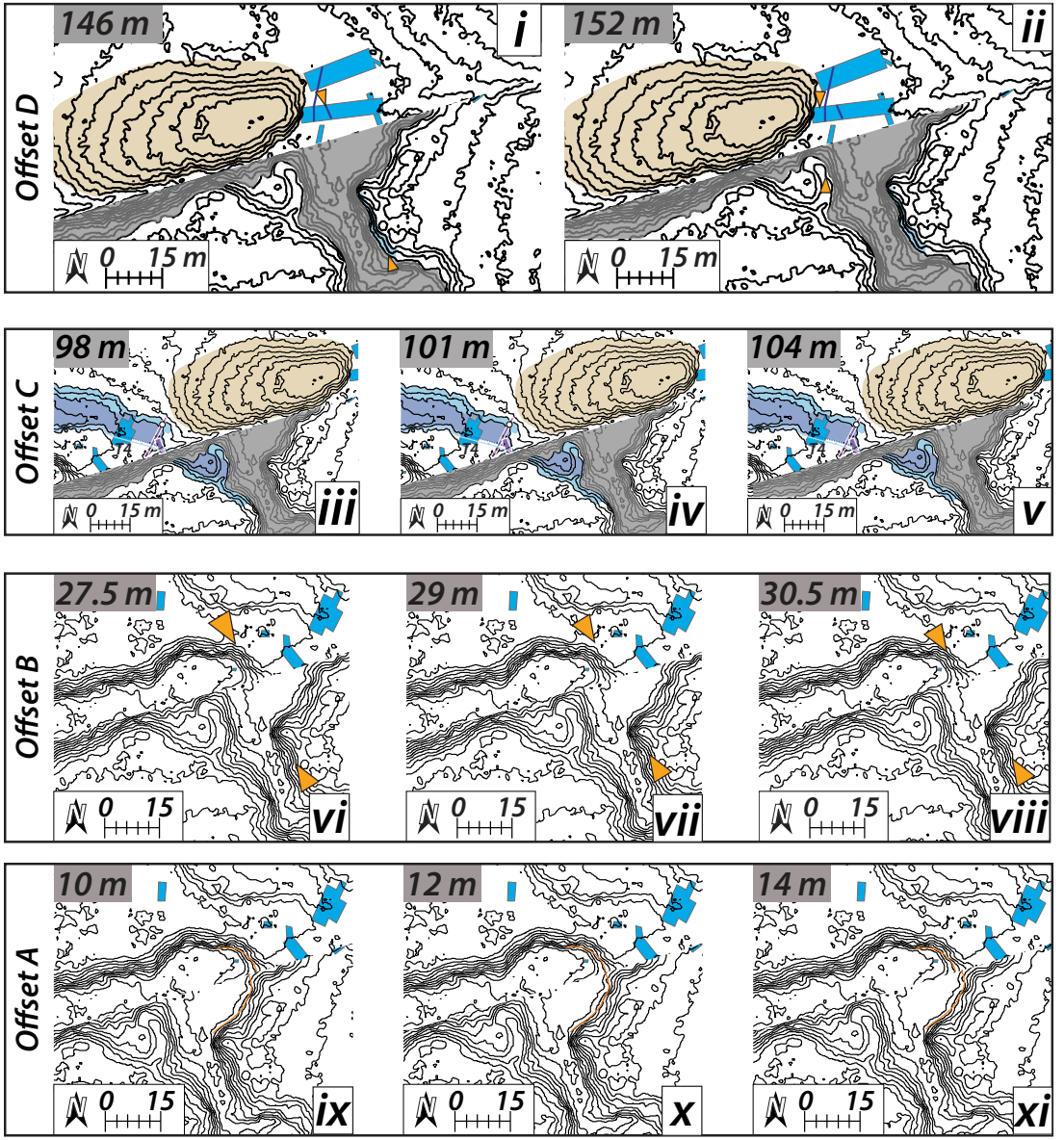

Figure 3. Restorations of downstream Loops Stream offsets (offsets A–D). In all panels, the topographic contour interval is 50 cm and is derived from lidar-acquired topographic data. Offset D panel shows minimum restoration at 146 m (i) and maximum restoration at 152 m (ii). Dark blue lines show channel C3 banks as excavated in trenches T-7 and T-10. Orange triangles show piercing points for minimum and maximum restorations. Beige shading highlights the shutter ridge. Gray shading shows areas that have been eroded since activity of channel C3. Offset C panel shows minimum restoration at 98 m (iii), preferred restoration at 101 m (iv), and maximum restoration at 104 m (v). Blue boxes indicate trench excavations. Northeast-southwest–trending purple rectangle shows the McMorran (1991) auger profile; NNW-SSE–trending purple rectangle shows the McMorran (1991) trench. Light blue shading indicates channel banks at time of initial incision of channel C2. Indigo shading represents the channel floor. Light blue solid line connects observations of the southwestern edge of channel C2; darker blue dotted line aligns thalweg features. White circle represents the northeastern channel edge exposed in the McMorran (1991) auger profile. Beige shading highlights the shutter ridge. Gray shading shows areas that have been eroded since activity of channel C3. Offset B panel shows minimum restoration at 27.5 m (vi), preferred restoration at 29 m (vii), and maximum restoration at 31.5 m (viii). Blue boxes show trench and pit excavations. Orange triangles highlight piercing points. Offset A panel shows minimum restoration at 10 m (ix), preferred restoration at 12 m (x), and maximum restoration at 14 m (xi). Blue boxes show trench and pit excavations. Orange lines highlight the natural curvature of the channel walls at last local incision of channel C1, mapped using the preferred restoration (offset B panel).

the Loops Stream headwaters <1 km to the east. Age data for all radiocarbon samples, including reworked samples that were not incorporated into our final OxCal age model, are presented in Table 1.

Channel C3 and Offset D

Channel C3 Location, Geometry, and Stratigraphy

The largest of the four Loops Stream channel offsets we identify (offset D) is constrained by a combination of: (1) the preserved geomorphic expression of the now–partly buried channel course incised into the S1 surface along the downstream reach north of the fault; and (2) three-dimensional (3-D) exposures of the now-buried channel C3 deposits, including the erosional base of the channel and basal bedload gravels, in two fault-parallel trenches we excavated just north of (i.e., downstream from) the fault (Fig. 3, offset D panel).

Despite the fact that the incised course of channel C3 north of the fault has been partially filled in by post–high energy streamflow deposits (see trench results in Fig. 4), the ~20-m-wide downstream channel course is well preserved in the landscape north of the fault, where it is marked by discontinuous, ~1-m-tall remnants of the paleochannel walls where the channel incised into surface S1. The geomorphically defined channel walls indicate that the channel flowed northward across the fault before turning sharply to the west around the eastern nose of a 3-m-tall, 20-m-wide bedrock shutter ridge that extends for ~70 m along the fault (Fig. 2D). Farther west, the location of the geomorphically defined channel C3 course indicates that the downstream end of the channel flowed westward along a stream course that was subsequently reoccupied and more deeply incised by channel C2, a younger channel course that will be discussed below as part of offset C. The partially buried downstream course of channel C3 is beheaded at the fault.

To better define the stratigraphy of the C3 channel and the underlying and overlying deposits, as well as the geometry and location of C3 where it crossed the fault, we excavated two fault-parallel trenches (T-7 and T-10) just north of the fault crossing near the eastern end of the bedrock shutter ridge around which the channel flowed (Fig. 4). Both trenches exposed the erosional base of the channel, as well as the C3 channel high-energy bedload gravel deposits (dark gray units in Fig. 4) and overlying predominantly fine-grained, post–channel abandonment deposits that have partially filled in the incised channel course (pale gray units in Fig. 4) . The C3 channel basal bedload deposits consist of brown, organic-rich, clast-supported pebble gravels. The gravel clasts are typically subangular and are infilled by a silty sandy matrix. Channel C3 bedload gravels onlap the eroded channel base where the channel incised into the eastern end of the bedrock shutter ridge, as seen on the western ends of the trench T-10 logs (Figs. 4B and 4C). Comparison of the elevations of the S1 fill-terrace surface and the erosional base of the C3 channel in trench T-7 indicates that the channel incised ~3 m down into the S1 surface. Channel C3 eroded down into an older unit consisting of angular to subangular, closely packed, clast-supported pebble gravel. This older, matrix-poor gravel does not exhibit any characteristics of significant fluvial transport (e.g., channelization, bedding, clast imbrication), suggesting that this gravel deposit may represent colluvium shed from the steep slope of the shutter ridge to the west of T-7 and T-10.

Both trenches document a fundamental shift in deposition at the top of the channel C3 basal bedload gravels. The C3 bedload gravels in both trenches T-7 and T-10 are overlain by gravelly sand deposits ~20 cm thick. Overlying these deposits in both trenches is a sequence of much finer-grained deposits, consisting mostly of silts and clays, with minor sparse gravel distributed through some beds. These fine-grained units are organic rich in places and contain 1- to 50-cm-long pieces of wood, including intact tree trunks and branches. Finally, the uppermost (~50 cm) of trenches T-7 and T-10 contains thinly bedded peats that have undulatory contacts, perhaps suggesting that these layers were deformed by liquefaction processes during local earthquakes.

In addition to defining the stratigraphy, trenches T-7 and T-10 constrain the fault-proximal depositional geometry of channel C3. Trench T-10 exposed both banks of channel C3, whereas trench T-7 revealed only the western incised bank of channel C3; the eastern bank of the stream lies somewhere to the east of the eastern end of the trench (Fig. 4). The 345°–350° trend of the incised channel walls and thalweg, as measured in 3-D in the trenches, is in good agreement with the C3 trend measured using the high-resolution lidar topography data, and is plotted as navy-blue lines in Figure 3 (offset D panel). The channel width of C3 is narrow in trench T-10 just north of the fault (see meter marker ~2–6 m in Figs. 4B and 4C), and increased to at least 8 m as the stream flowed around the eastern end of the shutter ridge, as shown by the minimum extent of the channel C3 bedload gravels exposed in trench T-7 (see distance ~3–12 m in Fig. 4A).

South of the fault, the only possible upstream source channel for the downstream reach of channel C3 described above is the currently active Loops Stream channel (Fig. 2). In the area immediately to the south of the fault, post–channel C3 streamflow associated with subsequent Loops Stream downcutting during progressive fault offset (discussed in following sections) has eroded the channel area south of the fault and east of the interpreted initial incision of C3, which is expressed in the geomorphology as a highly linear, north-northwest–trending upstream incised drainage.

Age Control for Channel C3 and Associated Deposits

To constrain the ages of channel C3 initiation and abandonment, we collected radiocarbon and luminescence samples from (1) the basal, pre–channel C3 gravels that C3 incised into, (2) the C3 channel bedload gravels, and (3) the post–channel abandonment fine-grained deposits, in trenches T-7 and T-10 (Table 1). Samples that yielded ages that were older than those recovered from underlying units were considered to be due to reworked material and were not included in our final age model.

Our final OxCal age model for the stratigraphy exposed in trenches T-7 and T-10 included 19 radiocarbon samples and two post-IR-IRSL samples,

TABLE 1. HOSSACK STATION RADIOCARBON DATA

Field information			Keck AMS data						OxCal calibrated, unmodeled ages ("R_Date")					
Sample name	Trench or pit number	Material	Fraction modern	±	$D^{14}C$ (‰)	±	^{14}C age (yr B.P.)	±	Maximum age (yr B.P.)	Minimum age (yr B.P.)	Maximum age (ka)	Minimum age (ka)	Calibrated age CE	
HS15-P7-1	7	Organic-rich mud	0.9742	0.0016	–25.8	1.6	210	15	285	146	0.354	0.215	1665	1804
HS15-P7-2	7	Organic-rich mud	0.9745	0.0016	–25.5	1.6	205	15	285	144	0.354	0.213	1665	1806
HS15-P7-3	7	Organic-rich mud	0.9789	0.0016	–21.1	1.6	170	15	275	—	0.344	—	1675	—
HS15-3	7	Bark	0.5544	0.0010	–445.6	1.0	4740	15	5577	5322	5.646	5.391	–3627	–3372
HS15-4-a	1	Charcoal	0.4112	0.0009	–588.8	0.9	7140	20	7979	7851	8.048	7.920	–6029	–5901
HS15-P7-4	7	Wood	1.0157	0.0018	15.7	1.8	–120	15	—	–210	—	–0.141	—	2160
HS15-4	5	Charcoal	0.5948	0.0011	–405.2	1.1	4175	15	4820	4536	4.889	4.605	–2870	–2586
HS15-P7-5	7	Wood	0.7301	0.0012	–269.9	1.2	2525	15	2722	2440	2.791	2.509	–772	–490
HS15-5	4	Wood	0.5141	0.0010	–485.9	1.0	5345	20	6185	5992	6.254	6.061	–4235	–4042
HS15-P7-6	7	Charcoal	0.6994	0.0087	–300.6	8.7	2870	100	3211	2754	3.280	2.823	–1261	–804
HS15-6	4	Organic-rich mud	0.8135	0.0083	–186.5	8.3	1660	90	1710	1320	1.779	1.389	240	630
HS17-7	10	Wood	0.3224	0.0009	–677.6	0.9	9095	25	10,247	10,188	10.316	10.257	–8297	–8238
HS15-P7-7	7	Charcoal	0.5937	0.0010	–406.3	1.0	4190	15	4823	4579	4.892	4.648	–2873	–2629
HS15-7	4	Organic-rich mud	0.7036	0.0012	–296.4	1.2	2825	15	2953	2795	3.022	2.864	–1003	–845
HS17-8	10	Wood	0.3532	0.0009	–646.8	0.9	8360	25	9449	9149	9.518	9.218	–7499	–7199
HS15-P7-8	7	Charcoal	0.5977	0.0010	–402.3	1.0	4135	15	4808	4450	4.877	4.519	–2858	–2500
HS15-8	4	Wood	0.8113	0.0014	–188.7	1.4	1680	15	1585	1488	1.654	1.557	365	462
HS15-P7-9	7	Wood	0.4052	0.0008	–594.8	0.8	7255	20	8155	7959	8.224	8.028	–6205	–6009
HS15-9	4	Organic-rich mud	0.7126	0.0013	–287.4	1.3	2720	15	2844	2750	2.913	2.819	–894	–800
HS15-P7-10	7	Wood	0.4458	0.0008	–554.2	0.8	6490	15	7427	7316	7.496	7.385	–5477	–5366
HS15-10	7	Charcoal	0.8631	0.0077	–136.9	7.7	1180	80	1269	918	1.338	0.987	681	1032
HS15-P7-11	7	Wood	0.2840	0.0007	–716.0	0.7	10,110	20	11,760	11,404	11.829	11.473	–9810	–9454
HS15-11	4	Wood	0.6452	0.0011	–354.8	1.1	3520	15	3834	3648	3.903	3.717	–1884	–1698
HS15-P7-12	7	Wood	0.3775	0.0008	–622.5	0.8	7825	20	8626	8458	8.695	8.527	–6676	–6508
HS15-12	7	Wood	0.3698	0.0007	–630.2	0.7	7990	20	8979	8647	9.048	8.716	–7029	–6697
HS15-13	7	Wood	0.3528	0.0008	–647.2	0.8	8370	20	9446	9268	9.515	9.337	–7496	–7318
HS17-14	10	Wood	0.3071	0.0009	–692.9	0.9	9485	25	10,754	10,581	10.823	10.65	–8804	–8631
HS15-14	7	Wood	0.3659	0.0009	–634.1	0.9	8075	20	9015	8777	9.084	8.846	–7065	–6827
HS15-15	7	Wood	0.9508	0.0016	–49.2	1.6	405	15	495	328	0.564	0.397	1455	1622
HS17-16	10	Charcoal	0.3168	0.0029	–683.2	2.9	9230	80	10,566	10,223	10.635	10.292	–8616	–8273
HS15-16	9	Charcoal	1.0287	0.0018	28.7	1.8	–220	15	—	–310	—	–0.241	—	2260
HS15-18A	9	Wood	0.9528	0.0016	–47.2	1.6	390	15	490	325	0.559	0.394	1460	1625
HS15-18B	9	Charcoal	0.9492	0.0018	–50.8	1.8	420	20	500	330	0.569	0.399	1450	1620
HS15-20	9	Charcoal	0.9563	0.0047	–43.7	4.7	360	40	486	305	0.555	0.374	1464	1645
HS17-21	10	Wood	0.5956	0.0012	–404.4	1.2	4165	20	4815	4529	4.884	4.598	–2865	–2579
HS15-21	4	Wood	0.7574	0.0014	–242.6	1.4	2230	15	2309	2150	2.378	2.219	–359	–200
HS15-22	4	Wood	0.7490	0.0012	–251.0	1.2	2320	15	2350	2185	2.419	2.254	–400	–235

(*continued*)

TABLE 1. HOSSACK STATION RADIOCARBON DATA (*continued*)

Field information			Keck AMS data						OxCal calibrated, unmodeled ages ("R_Date")					
Sample name	Trench or pit number	Material	Fraction modern	±	$D^{14}C$ (‰)	±	^{14}C age (yr B.P.)	±	Maximum age (yr B.P.)	Minimum age (yr B.P.)	Maximum age (ka)	Minimum age (ka)	Calibrated age CE	
HS17-23	10	Charcoal	0.3312	0.0010	–668.8	1.0	8875	25	10,151	9707	10.220	9.776	–8201	–7757
HS15-23	4	Wood	0.8546	0.0016	–145.4	1.6	1260	15	1180	1071	1.249	1.14	770	879
HS15-24	4	Wood	0.7979	0.0014	–202.1	1.4	1815	15	1735	1611	1.804	1.680	215	339
HS15-25	4	Wood	0.7321	0.0013	–267.9	1.3	2505	15	2709	2379	2.778	2.448	–759	–429
HS15-26	4	Wood	0.7416	0.0012	–258.4	1.2	2400	15	2460	2334	2.529	2.403	–510	–384
HS17-26	10	Seed	0.3601	0.0010	–639.9	1.0	8205	25	9251	9012	9.320	9.081	–7301	–7062
HS15-27	4	Wood	0.7389	0.0012	–261.1	1.2	2430	15	2675	2346	2.744	2.415	–725	–396
HS15-28	4	Plant material	0.7377	0.0014	–262.3	1.4	2445	15	2678	2350	2.747	2.419	–728	–400
HS15-29	4	Wood	0.7776	0.0016	–222.4	1.6	2020	20	1999	1888	2.068	1.957	–49	62
HS17-30	10	Charcoal	0.3581	0.0009	–641.9	0.9	8250	25	9277	9032	9.346	9.101	–7327	–7082
HS15-31	4	Charcoal	0.9206	0.0015	–79.4	1.5	665	15	649	555	0.718	0.624	1301	1395
HS15-32	4	Wood	0.6964	0.0013	–303.6	1.3	2905	20	3069	2878	3.138	2.947	–1119	–928
HS17-33	10	Seed	1.0473	0.0061	47.3	6.1	Modern	Modern	135	124	0.204	0.193	1815	1826
HS15-33	4	Wood	0.6986	0.0012	–301.4	1.2	2880	15	3035	2863	3.104	2.932	–1085	–913
HS15-34	4	Wood	0.5478	0.0034	–452.2	3.4	4835	55	5644	5326	5.713	5.395	–3694	–3376
HS15-35	4	Wood	0.5142	0.0009	–485.8	0.9	5345	15	6182	5995	6.251	6.064	–4232	–4045
HS17-35	10	Charcoal	0.1363	0.0013	–863.7	1.3	16,010	80	19,520	19,013	19.589	19.082	–17,570	–17,063
HS15-36	3	Charcoal	0.5975	0.0010	–402.5	1.0	4135	15	4808	4450	4.877	4.519	–2858	–2500
HS15-48	4	Wood	0.5140	0.0009	–486.0	0.9	5345	15	6182	5995	6.251	6.064	–4232	–4045
HS15-49	4	Wood	0.5125	0.0010	–487.5	1.0	5370	20	6202	5998	6.271	6.067	–4252	–4048
HS15-50	4	Charcoal	0.5759	0.0031	–424.1	3.1	4435	45	5276	4851	5.345	4.920	–3326	–2901
HS15-51	4	Wood	0.5137	0.0010	–486.3	1.0	5350	20	6185	5994	6.254	6.063	–4235	–4044
HS15-52	4	Wood	0.5156	0.0009	–484.4	0.9	5320	15	6180	5944	6.249	6.013	–4230	–3994
HS15-54	4	Charcoal	0.5991	0.0011	–400.9	1.1	4115	15	4800	4441	4.869	4.510	–2850	–2491
HS15-56	4	Wood	0.6455	0.0010	–354.5	1.0	3515	15	3833	3645	3.902	3.714	–1883	–1695
HS15-57	4	Wood	0.6941	0.0011	–305.9	1.1	2935	15	3144	2946	3.213	3.015	–1194	–996
HS15-58	3	Charcoal	0.6158	0.0012	–384.2	1.2	3895	20	4408	4156	4.477	4.225	–2458	–2206
HS15-59	3	Wood	0.7026	0.0011	–297.4	1.1	2835	15	2960	2798	3.029	2.867	–1010	–848
HS15-63	3	Wood	0.7056	0.0012	–294.4	1.2	2800	15	2925	2779	2.994	2.848	–975	–829
HS15-64	3	Wood	0.7078	0.0012	–292.2	1.2	2775	15	2875	2765	2.944	2.834	–925	–815
HS15-65	3	Wood	0.7098	0.0012	–290.2	1.2	2755	15	2856	2760	2.925	2.829	–906	–810
HS15-66	3	Charcoal	0.5483	0.0044	–451.7	4.4	4830	70	5651	5322	5.720	5.391	–3701	–3372
HS15-67	3	Wood	0.9329	0.0032	–67.1	3.2	560	30	556	505	0.625	0.574	1394	1445

Notes: Keck AMS is the name of the facility at UC Irvine that ran the samples. AMS stands for Accelerator Mass Spectrometer. OxCal is the community standard model and the method is discussed in the text (Bronk Ramsey [2009]). R_Date refers to the specific calculation (command) completed in OxCal. ± refers to 2σ. 1. Negative ages represent B.C.E. ages (as opposed to positive ages representing C.E.) in the final column, or represent the incorporation of extremely young radiocarbon in the yr BP columns. dashes indicate the model could not confidently converge on these values. Only radiocarbon data are included in this table. IRSL data are in the Supplemental Information (see text footnote 1). See discussion in text and log figures regarding which samples were included or excluded.

which we describe from oldest to youngest (Fig. 5A). Two luminescence samples from the pre–channel C3 gravels into which the C3 channel incised yielded late Pleistocene ages of ca. 24 ka (samples HS15-L-16 from trench T-7 [24.1 ± 1.5 ka] and HS17-L-01 from trench T-10 [24.0 ± 1.9 ka]) (see Section S1 in the Supplemental Material (footnote 1) for details on luminescence age determinations). Radiocarbon sample HS17-35, also collected from the pre–channel C3 gravel (trench T-10), yielded a slightly younger age of ca. 19 ka (19.082–19.589 ka). We dated 16 radiocarbon samples from the overlying channel C3 bedload gravel deposit from both walls of trench T-10 as well as the north wall of trench T-7. These samples from the C3 channel bedload gravels are significantly younger than the underlying gravels into which channel C3 was incised. Specifically, the oldest sample from near the base of the channel C3 bedload gravels (sample HS15-P7-11, collected from trench T-7) yielded an age of 11.473–11.829 ka, and the youngest sample collected from the C3 channel bedload gravels (sample HS15-P7-12, collected from trench T-7, ~10 cm stratigraphically above the level of sample HS15-P7-11) yielded an age of 8.527–8.695 ka. We exclude sample HS15-P7-11 from the trench T-7 and T-10 age model because this sample is ~2–3 k.y. older than underlying samples from the same unit, indicating that this sample is older than the depositional age of the unit. Most samples collected from the channel C3 bedload gravel unit, which are stratigraphically above sample HS15-P7-11 (i.e., samples HS15-13 [9.337–9.515 ka; trench T-7], HS15-12 [8.716–9.048 ka; T-7], HS15-14 [8.846–9.084 ka; T-7], HS17-26 [9.081–9.320 ka; trench T-10], and HS17-8 [9.218–9.518 ka; T-10]), were collected from similar stratigraphic depths in the two trenches and yielded similar ages. The similarity of these ages suggests that there had been minimal reworking and that the samples had incorporated little pre-depositional material. To minimize the effect of skewing the incision age in the younger direction based on radiocarbon material that was included in the channel following initial incision, we select the oldest of these sample ages—that of sample HS15-13—to be the representative sample dating the initial incision of channel C3 at 9.337–9.515 ka.

A younger sample, HS15-P7-10 (7.385–7.496 ka), was collected from a gravelly sand unit that overlies the basal channel C3 bedload gravels. Samples collected from the post-channel C3 abandonment clays and silts include HS15-3 (5.391–5.646 ka; trench T-7), HS17-21 (4.598–4.884 ka; trench T-10), HS15-P7-8 (4.519–4.877 ka; T-7), HS15-P7-7 (4.648–4.892 ka; T-7), HS15-P7-6 (2.823–3.280 ka; T-7), HS15-P7-5 (2.509–2.791 ka; T-7), HS15-P7-3 (<0.344 ka; T7), HS15-P7-2 (0.213–0.354 ka; T-7), and HS15-P7-1 (0.215–0.354 ka; T-7). The oldest and deepest of these samples stratigraphically above C3 channel gravels, sample HS15-3, was collected from <5 cm above C3 gravels within an overlying silty clay. Combining the age of this sample with the age of the shallowest sample from the underlying C3 gravel yields an OxCal boundary age for abandonment of channel C3 high-energy streamflow of 5.530–7.411 ka.

Restoration of Channel C3 and Offset D

As noted above, the downstream reach of channel C3 is beheaded at the fault, indicating that the upstream part of the original C3 channel has been offset right-laterally by Hope fault slip. The only

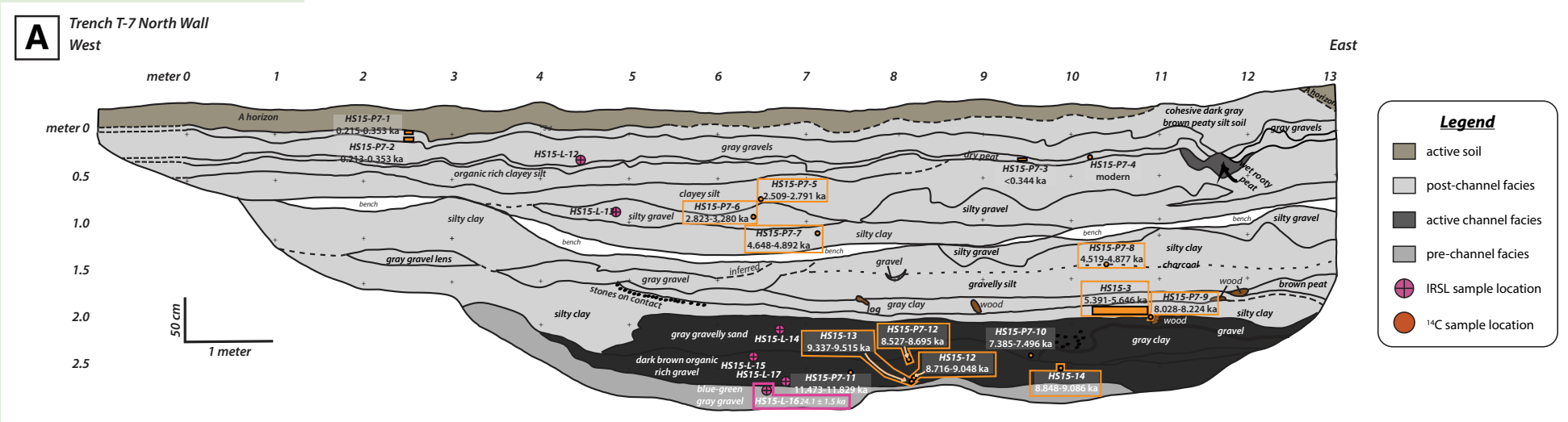

Figure 4. Line logs of trench T-7 north wall (A), trench T-10 north wall (B), and trench T-10 south wall (C). Darkest gray units denote C3 channel gravels. Medium gray units denote channel cut sequence, and lighter gray units denote channel abandonment facies. Radiocarbon samples (Table 1) are shown in orange, and infrared stimulated luminescence (IRSL; Supplemental Information [text footnote 1]) samples are shown in pink. All ages listed are calibrated and unmodeled and have 2σ error. Samples utilized in the composite age model discussed in this manuscript are boxed. (*Continued on following page.*)

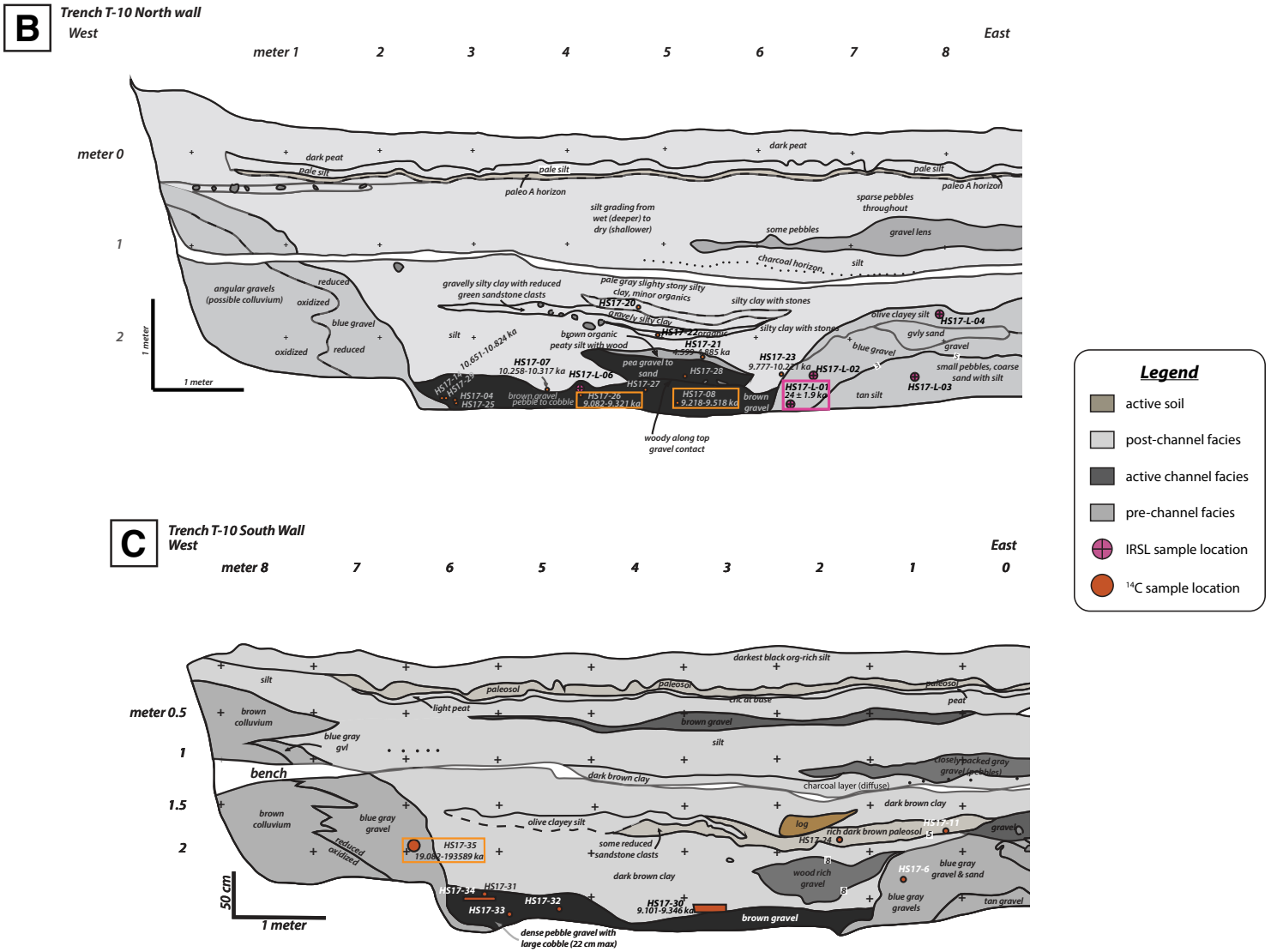

Figure 4 (*continued*).

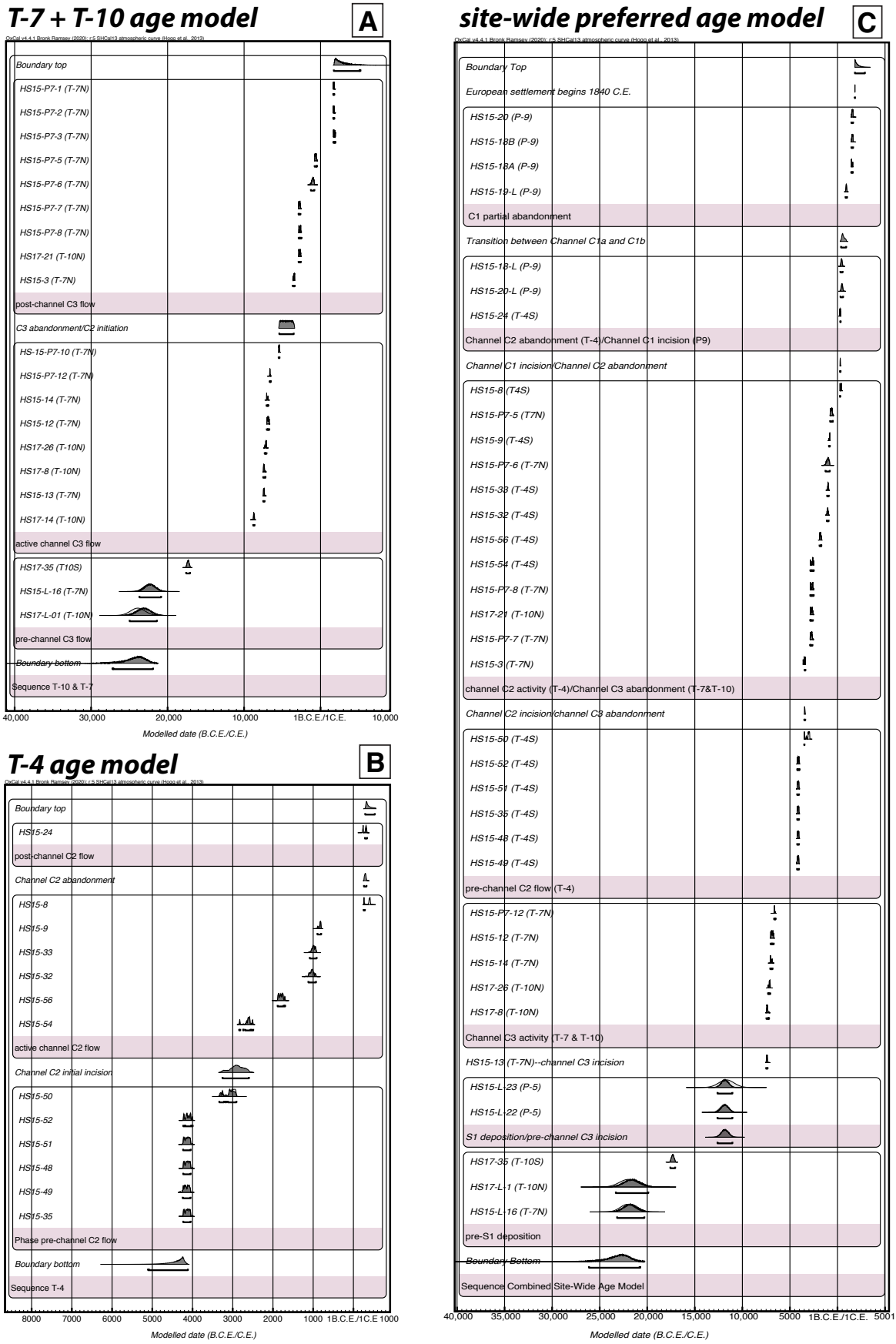

Figure 5. OxCal age models of trenches T-7 and T-10 (A) and trench T-4 (B), and a site-wide age model combining samples collected from all three trenches as well as from pits 5 and 9 (C). Lighter gray probability density function (PDF) for each sample denotes calibrated age, and darker gray PDF in front of lighter gray PDF shows the modeled 2σ age range. Trench number and wall direction if applicable follow sample numbers.

possible upstream (i.e., south of the fault) source drainage for the downstream reach of channel C3 is the currently active, deeply incised Loops Stream channel C1 (Fig. 3, offset D panel). Restoration of the two once-continuous offset channel segments allows us to determine the total displacement of the C3 channel since initial incision of the channel into the S1 surface ca. 9.4 ka. Key to this restoration is the use of the geomorphically defined limits of the location and geometry of initial incision of the upstream reach of the C3 channel into the S1 surface south of the fault. This part of the Loops Stream channel has been modified and eroded during subsequent channel-cutting episodes. Because of this erosion, we use the geometry of the topographically highest edges of the preserved western and eastern stream banks along the incised upstream reach of the Loops Stream, which record the widest-possible limits of initial incision into the S1 surface during channel C3 time when the stream was flowing through the downstream part of the channel exposed in trenches T-10 and T-7, to measure the maximum- and minimum-possible offsets of the C3 channel.

Specifically, we use these widest-possible limits on the location of the C3 channel upstream of the fault, together with the 3-D geometry of the C3 channel exposed in trench T-10 just downstream of the fault, to constrain the fault offset. The largest-possible offset is defined by restoring the western bank of the channel, as exposed in 3-D in both trenches T-7 and T-10 (blue line south of the orange triangle north of the fault on Fig. 3, offset D panel), to the current top of the western bank of channel C3 marking initial incision into the S1 valley-fill deposit south of the fault (note the nearly north-south topographic contour north of the orange triangle south of the fault on Fig. 3, offset D panel). The resulting maximum-possible offset of the western bank of channel C3 is 152 m. Similarly, to measure the smallest-possible offset of channel C3, we restore the trend of the incised eastern bank exposed in 3-D in trench T-10 (blue line south of orange triangle north of the fault on Fig. 3, offset D panel) relative to the north-northwest–trending, linear trend of the initial channel C3 incision into the S1 surface south of the fault (highlighted in pale blue shading north of the orange triangle south of the fault on Fig. 3, offset D panel). The resulting minimum-possible offset of the eastern bank of channel C3 is 146 m. Our "preferred" offset for the C3 channel of 149 m is simply the average of the minimum and maximum estimates of offset, given that subsequent incision and erosion by the Loops Stream has destroyed any further evidence of channel C3 in this area. The resulting offset is expressed as 149 ± 3 m.

Channel C2 and Offset C

Channel C2 Location, Geometry, and Stratigraphy

As with the older channel C3, the downstream segment of the C2 channel is beheaded at the fault. Downstream from the fault, the C2 paleochannel course is well preserved in the geomorphology, manifested by prominent, ~1-m-tall paleo–stream banks that are incised into the S1 surface (Fig, 3, offset C panel). These banks define an ~20-m-wide stream course extending west-northwestward (285°–295°) from the fault near the western end of the fault-parallel bedrock shutter ridge (Figs. 2C–2E; Fig. 3, offset C panel).

South of the fault, the topographically highest incision into the S1 surface to the west of the currently active C1 channel is marked by a linear edge trending 285°–290°, which is traceable for >30 m to where it merges upstream with the uppermost part of the deeply incised, southwestern bank of the active C1 channel (Figs. 2C–2E; Fig. 3, offset C panel). The linear paleo–stream banks preserved in the geomorphology north of the fault (west of the shutter ridge) and south of the fault (east of the shutter ridge, in present-day topography) are the only two stream-related geomorphic features at the Hossack Station site to exhibit an ~285° trend. All other stream-related features exhibit much more northerly trends near the fault. We therefore interpret the incised stream bank trending 285°–290° south of the fault as the upstream reach of the C2 channel, which is now offset from the downstream reach of C2 north of the fault.

We excavated trench T-4 approximately perpendicular to the geomorphically well-defined C2 channel course ~15 m north of the fault in order to expose the 3-D orientation of the C2 channel downstream of the fault, document the stratigraphy associated with C2 channel streamflow, and collect samples for dating (Fig. 6). Trench T-4 exposed a well-defined erosional channel cut, with the southwestern edge merging upward into the geomorphically defined C2 channel margin; we did not expose the northeastern margin of the C2 stream bank in trench T-4. The channel C2 clast-supported bedload gravel deposit filling in the base of this incised channel consists of subangular pebbles with a silt to sand matrix (dark gray units on Fig. 6). These gravels were incised into a flat-lying, well-bedded sequence of gravels and gravelly silts interspersed with silt and clay beds (medium gray units on Fig. 6). Overlying the C2 channel bedload gravels is a sequence of organic-rich clays and peats with local gravelly silt lenses (pale gray units on Fig. 6). As with our interpretation of the older C3 channel sequence exposed in trenches T-7 and T-10, we interpret this upward transition in trench T-4 from deposition of C2 channel bedload gravels to much finer-grained, organic-rich deposits as recording abandonment of high-energy streamflow through the C2 channel and subsequent post–channel abandonment deposition and partial infilling of the incised C2 channel by much lower-energy slack-water deposits.

Using exposures of the channel thalweg and southwestern edge of the incised C2 channel observed in both walls of trench T-4, we measured the trend of the C2 channel as 285°–290°. This is similar to the geomorphically defined trend of the southwestern channel margin between T-4 and the fault (pale blue line north of the fault in Fig. 3, offset C panel), as well as the trend of the interpreted southwestern margin of the C2 channel south (i.e., upstream) of the fault (pale blue line in Fig. 3, offset C panel). In addition, this northwestern trend of both the southwestern channel edge and thalweg of C2 is in good agreement with the trend of the same features documented by McMorran (1991) in a channel-perpendicular auger transect and trench located ~15 m east-southeast of trench T-4 (purple polygons in Fig. 3, offset C panel). We

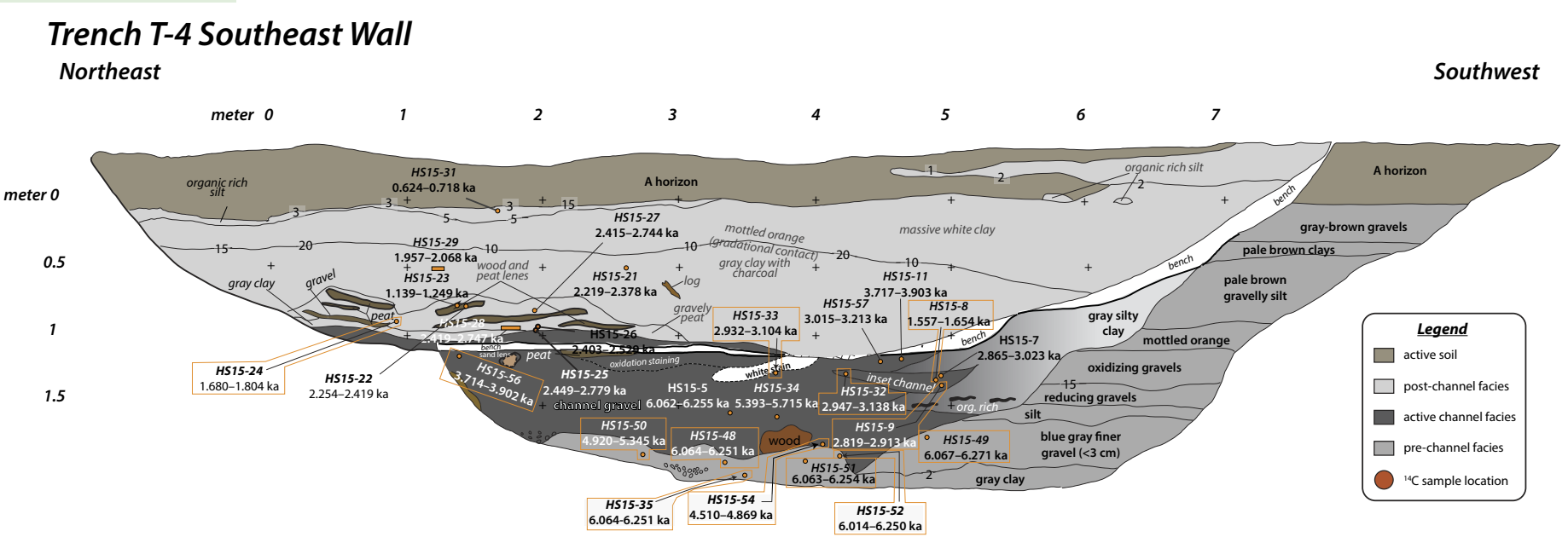

Figure 6. Line log of trench T-4 southeast wall. Darkest gray units denote C2 channel gravels. Medium gray units denote channel cut sequence, and lighter gray units denote channel abandonment facies. Radiocarbon samples are shown in orange. All ages listed are calibrated and unmodeled and have 2σ error (Table 1). Samples utilized in the composite age model discussed in this manuscript are boxed. Digits along contacts are uncertainty (in cm) of mapping the given contact.

projected the trends measured in the geomorphology and in our trench T-4 through the observation areas of McMorran (1991), and together these four observation areas confirm the orientation of the downstream reach of C2 north of the fault, which closely matches the northwestern trend of the topographic feature incised into the S1 surface south of the fault that we interpret as the southwestern channel bank of C2 upstream of the fault.

Age Control for Channel C2 and Associated Deposits

The oldest samples recovered from trench T-4 are from the horizontally bedded clastic units into which channel C2 incised (Fig. 5B). These radiocarbon samples include HS15-35 (6.064–6.251 ka), HS15-49 (6.067–6.271 ka), HS15-48 (6.064–6.251 ka), HS15-51 (6.063–6.254 ka), HS15-52 (6.013–6.249 ka), and HS15-50 (4.920–5.345 ka). The bedload gravels of channel C2 directly overly these pre–channel C2 incision samples. Sample HS15-54 (4.510–4.869 ka) was collected from near the base of the bedload gravels, ~2 cm above the erosional base of the C2 channel.

To determine the age of channel C2 incision as marked by the erosional base of the channel, we used OxCal to calculate the boundary age between sample HS15-50, collected from below the C2 channel bedload gravels, and overlying bedload gravel sample HS15-54. The resulting OxCal boundary age of 4.615–5.274 ka records initial incision of the C2 channel into the underlying deposits. This age of initial C2 channel incision is nearly contemporaneous with, but slightly younger than, the age of channel C3 abandonment recorded in trench T-7 (sample HS15-3; 5.391–5.646 ka).

Similarly, we can constrain the abandonment age of the C2 channel by using samples from higher in the bedload gravels in comparison with samples from the overlying fine-grained section. Younger samples collected from stratigraphically high in the C2 channel bedload gravels include samples HS15-33 (2.932–3.104 ka) and HS15-8 (1.557–1.654 ka). Several other samples collected from the channel C2 bedload gravels (e.g., sample HS15-5; 6.061–6.254 ka) yielded ages older than or contemporaneous with the samples collected from the underlying channel-cut facies. The age of sample HS15-8, which was collected from near the top contact of the channel C2 bedload gravels, is very similar to the 1.680–1.804 ka age of sample HS15-24, which was collected from near the base of the overlying organic-rich, post–channel abandonment fine-grained section. We calculate a boundary age of channel C2 abandonment between samples HS15-8 and HS15-24 of 1.693–1.756 ka.

Restoration of Channel C2 and Offset C

We use the 285°–295° trend of both the beheaded, downstream segment of the C2 channel and the upstream incised southwestern channel edge to reconstruct the offset of paleochannel C2. Specifically, restoration of the southwestern stream bank of channel C2, as preserved in the present-day geomorphology and observed in our trenches and McMorran's (1991) excavations, requires 101 m of back-slip to align the upstream and downstream segments of the channel trending 285°–295° (Fig. 3, offset C panel). The thalweg of channel C2 provides a secondary constraint on this offset (dashed darker blue line north of the fault on Fig. 3, offset C panel); the thalweg is poorly expressed in the geomorphology of the upstream channel segment.

The ±3 m uncertainty of our channel C2 restoration encompasses the full map width of the northeast-facing southwestern bank of C2 preserved south of the fault (Fig. 3, offset C panel). This error range takes into account measurement error when the southwestern bank was projected in the field, both within trench T-4 and from trench T-4 to the projected location of McMorran's (1991) long-since backfilled trench. The relatively small error range (±3 m) is due to the near-identical trends derived from the projection of multiple measurement points along the southwestern edge of channel C2 north and south of the fault in both the field as well as the high-resolution lidar topographic data that captured this same trend in the landscape.

Channel C1 and Offsets A and B

Channel C1 Location, Geometry, and Stratigraphy

Unlike older channels C2 and C3, the modern channel, channel C1, is not completely beheaded at the fault. Rather, the deeply incised C1 channel still accommodates active streamflow, albeit only along the westernmost part of the incised channel course at the fault crossing, where the channel makes a near-90° bend to the west (Figs. 2C, 2E). Channel C1 has incised ~5 m into the regional S1 surface, much more deeply than the older C2 and C3 channels. We interpret that this deep incision event, which occurred after abandonment of channel C2, was likely linked to local downstream relative base-level changes associated with the Hanmer River, the major, west-flowing river into which the Loops Stream flows ~1 km west of the study site (Figs. 2A, 2D). We recognize two offset channel configurations for the deeply incised C1 channel at the study site. We refer to these older channel geometries as C1A (younger) and C1B (older).

Channel C1B and C1A Location, Geometry, and Stratigraphy

South of the fault, the western edge of the deeply incised upstream reach of channel C1 is notably linear and extends NNW for >20 m to the fault crossing (Figs. 2C, 2E; Fig. 3, offset A and offset B panels). The eastern stream bank of channel C1 is similarly linear and parallel to the western bank from 15 to 30 m south of the fault. We refer to this highly linear upstream channel segment, which flowed northward almost perpendicular to the fault, as channel C1B. As discussed in a following section, restoration of this channel geometry defines offset B (Fig. 3, offset B panel).

Within ~15 m of the fault, the area to the east of where the linear upstream reach of the C1 channel would project has been eroded out down to the local (modern) C1A channel base level, indicating that this more recent erosion occurred after the initial deep channel C1 incision event associated with the linear channel C1B stream course (Fig. 3, offset B panel). North of the preserved linear upstream eastern stream bank, the edges of this eroded area are defined by the prominent, ~4–5-m-tall incised stream banks. The incised stream bank curves sharply to the east-northeast as it approaches the fault, and at the fault it turns sharply westward downstream, extending parallel to, and ~5–10 m north of, the Hope fault. This resulted in the development of a sharply curved, concave-to-the-southeast, incised stream bank at the fault crossing (Figs. 2C, 2E; Fig. 3, offset A panel). Streamflow along the east-northeast–trending upstream reach and through this sharp corner defines the geometry of channel C1A. As discussed in a following section, restoration of the offset of this stream geometry defines our youngest Offset A (Fig. 3, offset A panel).

We excavated a 1.5-m-deep pit (pit 9) into the protected, concave northeastern corner of the incised channel 1B course to document the stratigraphy and collect samples for dating the abandonment of bedload gravel deposition in this now low- to no-flow portion of channel C1 (Fig. 7). In his study, McMorran (1991) excavated a north-trending trench (his trench 2) in this same area; our pit 9 was hand dug ~3 m east of that earlier trench. The pit 9

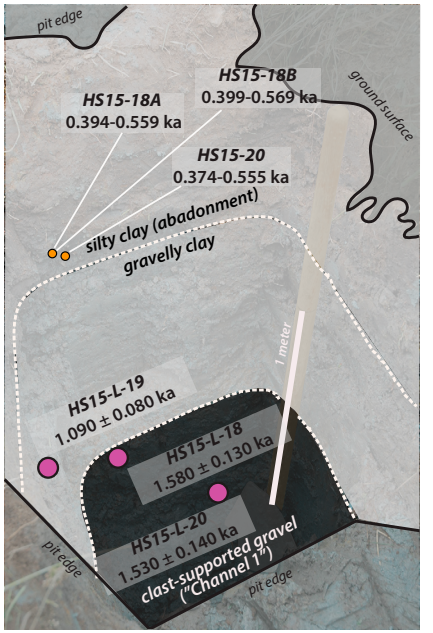

Figure 7. Annotated image of pit 9 exposure. Darkest gray units denote C1 channel gravels. Medium gray units denote channel cut sequence, and lighter gray units denote channel abandonment facies. Radiocarbon samples are shown in orange, and infrared stimulated luminescence samples are shown in pink. All ages listed are calibrated and unmodeled and have 2σ error (Table 1; Supplemental Material [text footnote 1]).

exposure revealed densely packed, coarse-pebble gravel below ~1 m depth, overlain along a sharply defined, planar contact by ~50 cm of massive, dark gray clayey sandy silt, which extended all the way upward to the base of the weakly developed A/C soil profile. As we discuss in the descriptions of the other Loops Stream offsets, we interpret this abrupt upward transition from high-energy fluvial gravel deposition to deposition of fine-grained muds indicative of very low-energy conditions as marking the abandonment of active, erosive streamflow with sufficient stream power to move gravel bedload, and subsequent passive infilling of the channel with fine-grained, suspended-load sediments.

Age Control for Channel C1B and Associated Deposits

The age of initial incision of channel C1 can be estimated from the timing of abandonment of flow through channel C2. This is implied by the lack of any other possible new channels that incised either northwest or north-northwest spatially between channels C2 and C1. Additionally, we observed evidence of channel C2 streamflow along the fault during progressive right-lateral defection of the channel during Hope fault offset. Specifically, there is a slight fault-parallel depression along the fault to the west of the geomorphic expression of the incised channel C2 (including trench T-4), indicating along-fault flow of channel C2. We exposed this channel in cross-section by excavating trench T-3 (Fig. S2 [footnote 1]). This trench exposed a fault-parallel (~075°) channel. Flow of channel C2 through trench T-3 supports a channel geometry in which channel C2 was flowing along the fault during its progressive right-lateral deflection by the Hope fault up until channel C2 abandonment and simultaneous initiation and incision of channel C1.

The age of C2 abandonment, the stream course that immediately predates the C1 channel course, is derived from sample HS15-24 collected from trench T-4, which yielded an age of ca. 1.5–1.6 ka. Samples were also collected from the C1 gravels that were exposed in pit 9, but we were unable to sample any deposit depositionally older than the C1 gravels. Therefore, any sample collected from pit 9 C1 gravels would represent a minimum age of C1 incision, whereas the age of C2 abandonment likely provides a more accurate estimate of C1 incision. Pit 9 C1 sample ages will be discussed in the section titled "Age Control for Channel C1A and Associated Deposits."

Restoration of Channel C1B and Offset B

Initial incision of channel C1 was oriented north-northwest and utilized the deeply incised upstream thalweg south of the fault. This upstream reach was first incised during channel C3 activity and was later reactivated during C1 incision. The eastern bank of this north-northwest incision is restored by back-slip of 29 m. This restoration aligns the eastern bank of C1 cutting across the fault as C1 begins to flow southwest parallel to the fault. Our ±1.5 m lateral uncertainty in the offset measurement encompasses ±1 m of potential elevation change in the eastern bank elevation across the fault (lateral uncertainty encompasses two contour lines on the 50 cm contour interval maps presented in Fig. 3, offset B panel). These error bounds provide the maximum and minimum values of sedimentologically plausible fault offset. Any offset restoration value smaller than this 29 ± 1.5 m range would result in initial channel incision having occurred during avulsion out of an east-northeast–flowing, fault-parallel "S" bend in the channel, a geometry that we consider to be sedimentologically implausible. We illustrate this unlikely geometry in Figure S3 (footnote 1), which shows the stream geometry that would be required if initial avulsion out of the C1 channel across the fault occurred at an offset restoration of 14 m. There is no preserved evidence, either in the geomorphology or in the trench logs, to support the idea that initial incision of channel C1 occurred in such an "S" shape. As such, we do not consider stream geometries that require <27.5 m offset restoration, which we consider to be the lower end of sedimentologically plausible stream geometry at the time of initial avulsion and incision of the C1B channel across the fault.

Age Control for Channel C1A and Associated Deposits

We collected two radiocarbon and three IRSL samples from pit 9 to constrain the age of most recent high-energy channel C1A streamflow through the site. The two charcoal samples (HS15-18 and HS15-20) were sampled from 46 cm depth from within the silty clay unit, <5 cm above the contact with the underlying 50-cm-thick gravelly clay unit, which in turn overlies the basal, high-energy bedload gravels. Collectively, samples HS15-18A, -18B, and -20 yielded an age range of 0.374–0.569 ka. Because these ages were collected from within the post–channel abandonment silty clays >50 cm stratigraphically above the channel bedload gravels exposed in the base of pit 9, they provide a conservative minimum age constraint of ca. 375–570 yr on the most recent high-energy streamflow across the site of pit 9.

One of the three IRSL samples (HS15-L-19) was collected from the gravelly silty clay at 98 cm depth just above the sharp contact with the underlying channel C1B bedload gravels, whereas the other two were collected from the uppermost bedload gravels (sample HS15-L-18 at 109 cm depth) and from deeper within the gravel deposit (sample HS15-L-20 at 138 cm depth) respectively. The post-IR-IRSL$_{225}$ ages calculated using the methodology of Rhodes (2015) yielded ages of 1.270 ± 0.190 ka (sample HS15-L-19), 3.500 ± 0.310 ka (sample HS15-L-18), and 4.940 ± 0.440 ka (sample HS15-L-20). The ages from the two lower samples are apparently out of stratigraphic order, given that these samples are older than the abandonment of channel C2 yet represent flow through the younger channel C1. Additionally, the single-grain age plots reveal a complicated distribution of ages suggestive of a continuum of partially bleached signals (Section S1 [footnote 1]). We suspect that samples HS15-L-18 and HS15-L-20 reflect a process known as "shadowing", in which the presence of numerous, apparently older grains were only partially or incompletely bleached during the youngest depositional event, which is the event of interest (i.e., flow through channel C1). Because these grains are only partially bleached, they do not record the younger age of interest, and instead make the calculated age apparently older because

these partially bleached grains cannot statistically be differentiated from the youngest grains, which likely date the depositional event of interest.

In order to overcome the limitations presented by incomplete bleaching and shadowing, the IR_{50} (see Supplemental Material [footnote 1]) signals, which are bleached in sunlight more rapidly, were examined for these two samples. For the uppermost sample (HS15-L-19), an IR_{50} age of 1.090 ± 0.080 ka was determined. The equivalent dose estimates for the IR_{50} and post-IR-$IRSL_{225}$ signals are well within 1σ uncertainty values of each other, indicating there is no significant difference between the two estimates. We have reasons to be confident in the thermal stability of the post-IR-$IRSL_{225}$ age demonstrated by comparison with independent age assessments at a range of different sites (Rhodes, 2015), and the apparent close agreement between these age estimates suggests no significant (i.e., beyond uncertainty limits) instability of the IR_{50} signal (i.e., fading) for grains in this catchment.

The IR_{50} ages of these samples are 1.580 ± 0.130 ka for HS15-L-18 and 1.530 ± 0.140 ka for HS15-L-20. Based on the confirmation of acceptable IR_{50} signal stability provided by sample HS15-L-19, we have confidence that the IR_{50} age estimates for the two lower samples within this section are representative of the youngest depositional (i.e., bleaching) event recorded by these gravel deposit and therefore represent timing of active flow through channel C1.

The IR_{50} age of deeper sample HS15-L-20 almost exactly matches the abandonment age of channel C2 documented independently in trench T-4, supporting the idea that the IR_{50} ages likely provide better estimates of the ages of the sediments in pit 9 (see Supplemental Material [footnote 1]. The IR_{50} ages would thus suggest that high-energy C1A channel flow was active by 1.5 ka and was abandoned at the location of pit 9 ca. 1.1 ka. Based on this, we have used the IR_{50} ages from pit 9 in our calculation of our youngest slip rates.

Restoration of Channel C1A and Offset A

The prominent curvature of the northeastern and northern banks of the channel C1 stream sharply offset by the Hope fault <5 m east of pit 9 defines offset A (Fig. 3, offset A panel). Our preferred restoration of the offset is 12 m, which restores the stream bank into a smooth, sedimentologically plausible configuration (Fig. 3, offset A panel). The ±2 m of lateral uncertainty in the offset measurement takes into account the small range of sedimentologically plausible orientations of this natural curve in the channel, as well as potential colluvial burial of the offset stream bank on the north side of the fault, which, if not accounted for, would result in an underestimate of the true offset.

Loops Stream Headwaters Region and Offset E

Loops Stream Headwaters Geomorphology and Channel Location and Geometry

In addition to the four progressive offsets of the Loops Stream at the main, western Hossack Station study site, we restore the larger, longer-term offset of the headwaters of the Loops Stream at the location where this channel initially incised <1 km east of offsets A–D (offset E; Fig. 8). As noted above, the broad valley at the Hossack Station site is marked by a planar, valley-wide abandoned floodplain of the Loops Stream that we refer to as surface S1. Following deposition of the valley-filling sequence capped by the S1 surface, which for simplicity we refer to as the S1 deposit, the Loops Stream incised into this surface, marking a change from valley-filling aggradation to incision that has been observed in numerous river systems throughout this part of New Zealand (e.g., Bull and Knuepfer, 1987).

The Loops Stream originates from a deep canyon that was incised by the southward-flowing headwaters of the stream (Figs. 2B, 8). This upstream headwaters drainage is now backfilled and aggraded upstream of a narrow, fault-bounded popup structure associated with a minor, secondary, northern splay of the Hope fault that crosses the headwaters drainage (Fig. 8). The incised Loops Stream channel has been offset right-laterally along the southern edge of this small popup structure by the main dextral strand of the Hope fault (Fig. 8). The stream now flows mainly westward, subparallel to the Hope fault, toward the main study area.

Stratigraphy of Valley-Filling S1 Gravels into Which Loops Stream Incised

To provide age control for the S1 surface into which the Loops Stream has incised, we excavated pit 5 into the aggradational S1 valley fill near the beheaded downstream channels of the Loops Stream (Fig. 9). This pit revealed that the valley-filling, aggradational deposit consists of clast-supported pebble gravel with rare cobbles, interbedded with minor, thin (5–8 cm thick) silty-sandy lenses and layers (Fig. 9). The matrix of the S1 bedload gravels is composed of medium-grained sand to silt.

These valley-filling gravels were exposed at ~40 cm depth in pit 5 (Fig. 9). They are overlain by a silty gravel, which is in turn overlain by a relatively clast-free silt in the uppermost ~15–20 cm extending up to the S1 surface. The silty gravels that immediately overlie the main, bedload gravels exposed in the pit likely represent sporadic reoccupation of the S1 surface as an active floodplain, likely in intermittent flooding events, following abandonment of consistent, high-energy streamflow across the S1 floodplain capable of transporting clast-supported bedload gravels. The clean silts that overlie the silty gravels record only low-energy conditions indicative of complete abandonment of the S1 floodplain.

Age Control for S1 Bedload Gravel Deposition and Abandonment

To provide age control for the abandonment age of bedload gravel deposition and post-abandonment stabilization of the S1 surface, we collected five IRSL samples and one radiocarbon sample from pit 5. IRSL sample HS15-L-23, collected from the main gravel package at 62 cm depth, yielded an age of 13.7 ± 1.6 ka. Sample HS15-L-22, collected from a deeper gravel deposit at 122 cm depth, yielded a very similar age of 13.9 ± 0.9 ka, indicating that high-energy S1 floodplain bedload gravel

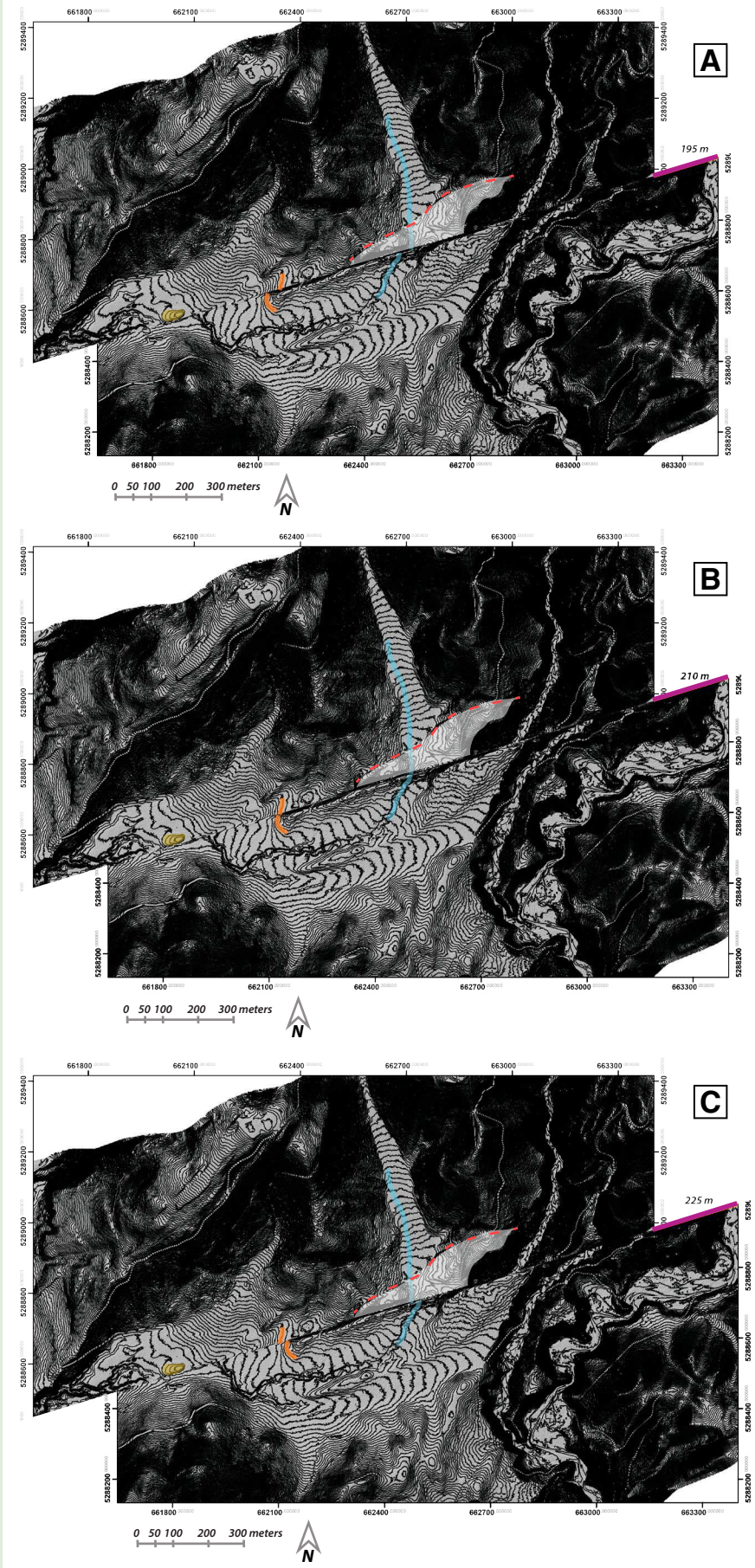

Figure 8. Restorations of offset E at 195 m (A), 210 m (B), and 225 m (C). Maps consist of 50 cm topographic contours overlaid on shaded-relief images of a digital elevation model. Topographic data used in this figure are from lidar dataset available referenced in manuscript. Orange line denotes nose of a bedrock ridge, and blue denotes the potential thalweg of the initial orientation of the Loops Stream. Shutter ridge adjacent to smaller, previously discussed offsets A–D is highlighted in light beige. Recent fault-parallel popup is shaded in white. Splay fault that likely aided in uplift of this block is denoted with a red dashed line. Graticule at map edges are in reference frame NZGD2000. Center of field of view in each panel ~ –42.537672°, 172.976185°.

deposition was active until ca. 13.8 ka. These latest Pleistocene, 13.5–14 ka ages are similar to ages collected from similar valley-filling aggradational gravels in other drainages within the Marlborough region (e.g., Zinke et al., 2017, 2019).

In addition to these bedload gravel ages from pit 5, we also collected IRSL sample HS15-L-24 from 33 cm depth within the gravelly silt, and charcoal sample HS15-4 from 25 cm depth in the post-abandonment silt. These samples yielded ages of 3.1 ± 0.2 ka and 4.605–4.889 ka, respectively, which significantly postdate the youngest bedload gravels.

Restoration of Hope Fault Offset of Loops Stream Headwaters

The right-lateral offset of the Loops Stream headwaters provides a well-defined restoration that defines the amount of post–S1 surface abandonment fault offset. Specifically, restoration of the incised Loops Stream by 210 m aligns the downstream segment of the stream with the southward-flowing headwaters canyon. As noted above, the stream immediately upstream of the main (southern) strand of the Hope fault has deeply incised into the fault-parallel popup structure associated with the secondary, northern strand of the fault. However, as shown in Figure 8, particularly in Figure 8B (preferred restoration), projection of the linear, upstream headwaters canyon across this subsequently uplifted area reveals a well-defined correlation of the upstream and downstream segments of the incised Loops Stream channel.

In addition to these piercing points, secondary piercing lines for restoration of post–S1 surface abandonment right-lateral Hope fault slip are recognized along the buttress unconformity between the bedrock valley walls and the onlapping aggradational gravels capped by the S1 surface downstream from the fault just west of the headwaters canyon (Fig. 8). Restoration of 210 m restores a northeast-trending bedrock ridge offset along the fault. The S1 deposits onlap the ridge, as best observed along the western margin of the ridge south of the fault (orange line highlights onlap contact in Fig. 8). Furthermore, restoration of this bedrock ridge aligns a wind gap south of the fault with a small depression north of the fault.

We assign error limits of ±15 m to the preferred 210 m offset of the Loops Stream headwaters based on the upper and lower limits of restorations that preserve the sedimentological plausibility of flow through the Loops Stream headwaters and through the downstream reach of the Loops Stream. Specifically, the restoration of the Loops Stream headwaters canyon with its downstream stream just south of the fault becomes notably nonlinear, with a distinct "S" bend at the fault, for restorations <195 m (Fig. 8A). We derive the same maximum +15 m error limit for the restoration of the offset onlap contact between the S1 deposit and the bedrock ridge ~100–200 m west of the Loops Stream headwaters; the topographic relationships in this area become sedimentologically implausible at restorations >225 m (Fig. 8C).

The youngest S1 terrace gravels at the Hossack Station study site are ca. 13.8 ka, as determined by samples HS15-L-22 and HS15-L-23 from the uppermost gravels sampled in pit 5. This age dates the youngest high-energy deposition of bedload gravels, marking the abandonment of the S1 fill terrace phase of aggradation. In our depositional model, this cessation of high-energy bedload gravel deposition is nearly contemporaneous with initial incision of the Loops Stream into the S1 surface. Thus, the age of these youngest S1 gravels provides a datum that predates, and likely closely dates, the onset of accumulation of right-lateral offset of the Loops Stream headwaters canyon measured as offset E. In addition to the transition from coarse gravels to silt noted in the pit 5 stratigraphy, the abandonment of S1 gravel deposition is marked by the top of the buttress unconformity of S1 gravels lapping onto a bedrock ridge (shown with orange outlines in Fig. 8). This depositional feature, which is related to last stages of S1 terrace bedload gravel aggradation, is directly dated by the youngest S1 terrace gravel ages. These youngest S1 terrace gravel ages are referred to as maxima because the younger constraining ages on S1 abandonment, collected from the overlying silty gravel (IRSL sample HS15-L-24; 3.1 ± 0.2 ka; 33 cm depth) and silt (charcoal ^{14}C sample HS15-4; 4.605–4.889 ka; ~25 cm depth), are significantly younger than the ages recovered from the underlying S1 gravel deposits. These age-offset relationships are discussed in detail in a later section in the context of their importance for constraining the slip rate based on offset E.

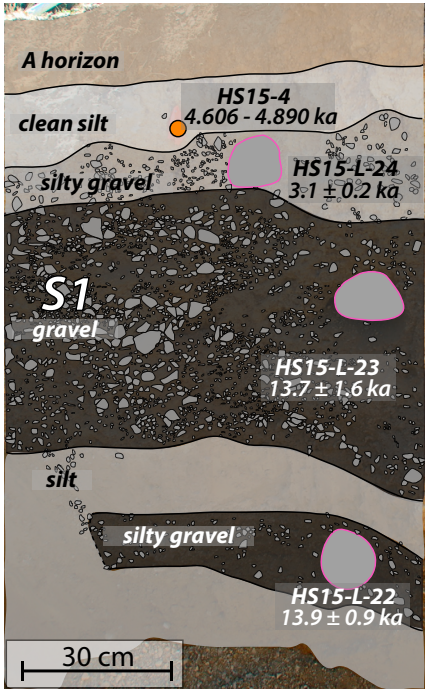

Figure 9. Annotated image of pit 5 exposure. Darkest gray color represents surface S1 gravel (valley-filling) deposit. Radiocarbon sample is shown in orange, and infrared stimulated luminescence samples are shown as pink open circles. All ages listed are calibrated and unmodeled and have 2σ error (Table 1; Supplemental Material [text footnote 1]).

SUMMARY OF PROGRESSIVE LOOPS STREAM FAULT OFFSETS

Composite Age Control

Following the initial OxCal modeling of the age data from each excavation, we present a single

depositional model incorporating and synthesizing all of the age data from the four western Loops Stream offset sites as well as the eastern headwaters offset site. Specifically, we use age data from trenches T-4, T-7, and T-10 as well as age data from pits 5 and 9 that constrain the ages of key depositional transitions, particularly the initiation and abandonment of individual Loops Stream channel segments during progressive fault offset (Fig. 5C). This model includes all ages from these excavations that were not reworked or out of stratigraphic order and that have been discussed above in sections about each individual offset. These ages were grouped into depositional phases pervasive at the Hossack Station site (e.g., S1 deposition; or channel C1 inactivity–channel C2 activity). Because we have temporally and depositionally correlated stratigraphy across trenches, we therefore combine ages from each trench exposure into one age model. For instance, pebble-cobble gravel deposits of channel C1 exposed in trenches T-7 and T-10 would be capped by fine-grained deposits, which represent the abandonment of channel C1 locally; the fine-grained deposits in trenches T-7 and T-10 are therefore contemporaneous with coarse gravel deposits of channel C2 exposed in trench T-4.

Based on this composite, site-wide age model, we estimate boundary ages (i.e., channel initiation and abandonment events) calculated between samples from different excavations. We use these ages from the composite age model when calculating incremental slip rates discussed in a later section. In the following section, we present our preferred interpretation of the Loops Stream evolution with accompanying ages calculated in this composite, site-wide age model presented in Figure 5C.

Loops Stream Evolution

Abandonment and initial incision of the S1 aggradational terrace surface began ca. 13.8 ka (Fig. 10A). This age is not modified in the composite age model because no other trench relative to P5 exposed such a young section of S1 deposits. Our preferred age for S1 deposition at the Hossack Station site is therefore based off of IRSL sample HS15-L-23 with an age of 13.7 ± 1.6 ka. This age has a wider error estimate than similarly aged sample HS15-L-22 collected from the S1 deposit exposed in pit 5. We favor the broader error of age of this sample because we have no direct constraint on a minimum (youngest possible) age of transition from S1 valley filling (aggradation) to Loops Stream initiation (incision) (see sample HS15-L-16 from trench T-7), although we suspect that the 13.8 ka age of the youngest gravel likely closely dates the transition from the end of terrace aggradation to initial incision of the S1 surface by the Loops Stream. Back-slip of 210 ± 15 m restores the initial geometry of the incised Loops Stream segment immediately downstream of the fault with its headwaters canyon (offset E).

The next-youngest channel offset configuration that we can constrain is the 149 ± 3 m offset of the C3 channel exposed in trenches T-7 and T-10 (Fig. 10B). The C3 channel initially flowed due north, nearly perpendicular to the fault, around the eastern corner of the fault-parallel bedrock ridge (offset D). Due to the young alluvial fan covering the S1 surface north of the fault for 100+ m between trenches T-7 and T-10 and the bedrock ridge that is restored in offset E, we do not know if there was a stream course older than C3 that flowed under this younger fan. Our preferred age of offset D is unchanged in this composite age model, and we continue to use the representative sample of HS15-13 (composite age model yields an age of 9.337–9.515 ka, i.e., ca. 9.4 ka) to date initial incision of C3 (see previous discussion of offset D). The C3 channel continued to be the active channel for ~50 m of Hope fault displacement, developing in the process a pronounced "S" bend along the fault (Fig. 10C).

High-energy streamflow through the deflected C3 channel continued from 9.4 ka until it was abandoned ca. 5.4 ka when the younger C2 channel cut across the fault along a northwesterly path ca. 5.4 ka (Fig. 10D). Initial incision of the C2 channel occurred near the western end of the fault-parallel shutter ridge. This shutter ridge apparently prevented any stream avulsion of the C3 channel during its increasing deflection by Hope fault slip, and the Loops Stream channel was not able to cut the next-younger, northwest-trending C2 channel geometry until Hope fault slip had deflected the upstream reach of the C3 channel westward past the western end of the bedrock ridge. Restoration of the initial ~285° geometry of the C2 channel at 101 ± 3 m indicates that the C2 channel was active from 9.4 to 5.4 ka, a time that spanned ~50 m of Hope fault displacement. We use sample HS15-3 (ca. 5.4–5.7 ka) from the abandonment facies of channel C3 exposed in trench T-7 as the youngest possible age of flow through C3, and sample HS15-50 (ca. 4.9–5.3 ka) from the terrace facies of channel C2 exposed in trench T-4 as the oldest possible age of incision of C2. The boundary age (achieved by using the *Boundary* function in OxCal) between these two samples is 5.409–5.503 ka. The age of channel C2 initial incision corresponds to offset C.

Continued flow through the C2 channel geometry following initial incision at ca. 5.4 ka results in another "S"-bend geometry with flow along the Hope fault (Fig. 10E). This inefficient flow path through the "S" bend was eventually abandoned, likely following a change in base level in the nearby Hanmer River. Once the bend was abandoned, channel C1 reincised deeper into the previously incised C3 flow path south of the fault. The age of C2 abandonment determined by the boundary between samples HS15-24 (trench T-4 fine-grained material overlying C2 channel gravels) and HS15-8 (trench T-4 youngest C2 gravel sample) of ca. 1.6 ka is very similar to the IR_{50} ages of C1 gravels exposed in pit 9 (sample HS15-L-18, 1.580 ± 0.130 ka; HS15-L-20, 1.530 ± 0.140 ka), again suggesting a direct transition from C2 flow to C1 (Fig. 10F). Sample HS15-L-19 (1.090 ± 0.080 ka) provides the youngest possible age of flow through the channel C1B flow path (i.e., C1 initial incision). Because the boundary age between samples HS15-L-19 and HS15-L-18 of 1.101–1.646 ka overlaps with the age of C1 incision on the older end, we favor the younger end of this error estimate and prefer to use the age of sample HS15-L-19 as a good estimate of channel C1B abandonment (Fig. 10G). Following the C1B channel course, channel C1A incised a curve in the Loops Stream at the fault (Fig. 10F). This bend geometry has been subsequently offset by 12 m following incision of this curved east bank (offset A).

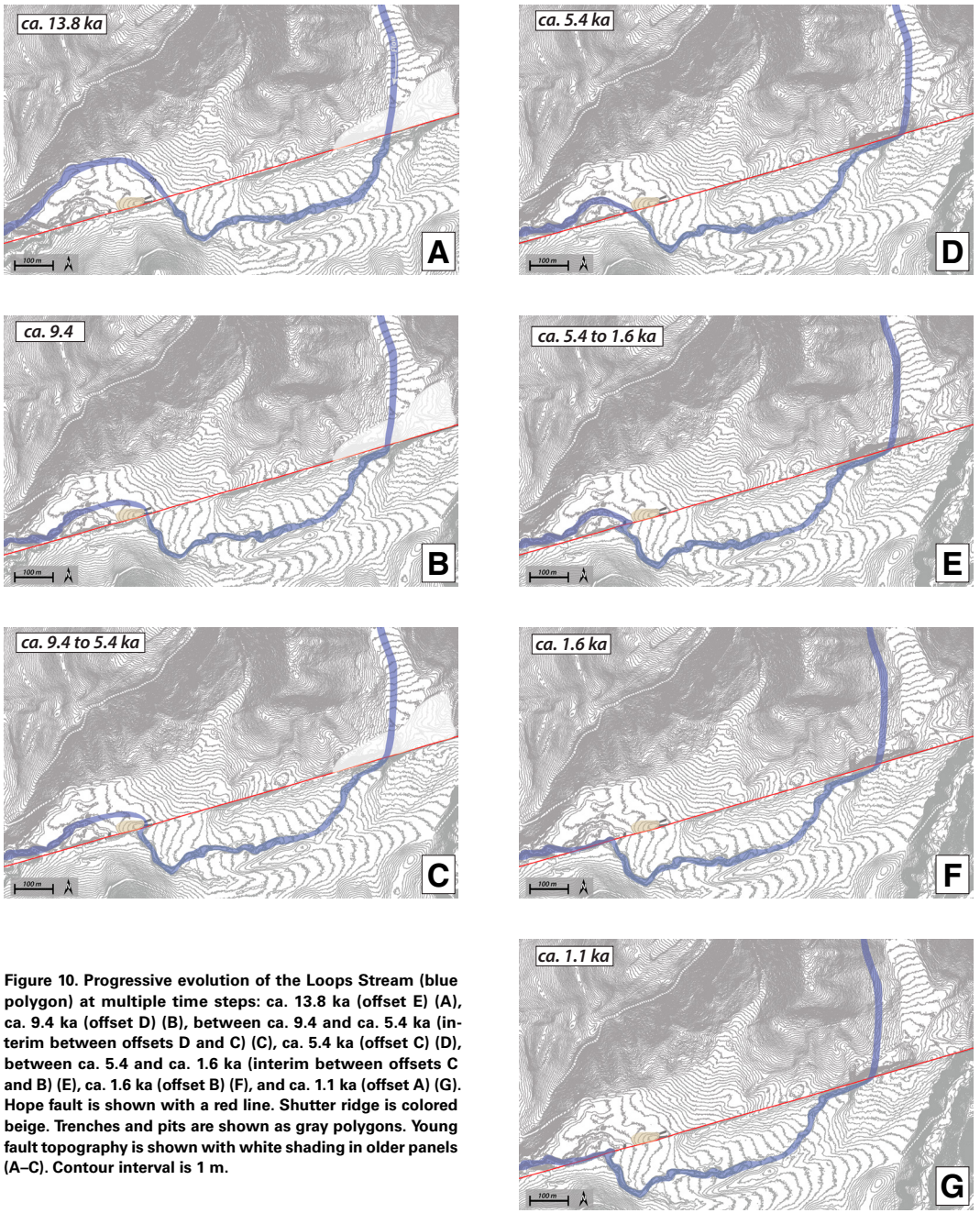

Figure 10. Progressive evolution of the Loops Stream (blue polygon) at multiple time steps: ca. 13.8 ka (offset E) (A), ca. 9.4 ka (offset D) (B), between ca. 9.4 and ca. 5.4 ka (interim between offsets D and C) (C), ca. 5.4 ka (offset C) (D), between ca. 5.4 and ca. 1.6 ka (interim between offsets C and B) (E), ca. 1.6 ka (offset B) (F), and ca. 1.1 ka (offset A) (G). Hope fault is shown with a red line. Shutter ridge is colored beige. Trenches and pits are shown as gray polygons. Young fault topography is shown with white shading in older panels (A–C). Contour interval is 1 m.

INCREMENTAL SLIP RATES

We calculate incremental slip rates over different time spans between channel initiation and abandonment events by combining the offset measurements with the absolute age control associated with each offset measurement (Fig. 11). We use a Markov chain–Monte Carlo approach for calculating slip rates and quantifying their associated errors (after Gold and Cowgill, 2011; Zinke et al., 2017, 2019). The Monte Carlo approach presented in this paper calculates errors in 2σ.

Using this method, we calculate the slip rate between offset E and offset D (slip rate DE) (from 13.8 to 9.4 ka; from 210 to 149 m) as 13.7 +4.0/–3.4 mm/yr, slip rate CD (between offsets C and D) (9.4 – 5.4 ka; 149 – 101 m) as 12.0 ± 0.9 mm/yr, slip rate BC (5.4 – 1.6 ka; 101 – 29 m) as 19.1 ± 0.8 mm/yr, slip rate AB (1.6 – 1.1 ka; 29 – 12 m) as 32.7 +~124.9/–10.1 mm/yr, and slip rate from offset A to the origin (OA) (1.1 ka to 2019 CE; 12 – 0 m) as 8.2 +2.7/–1.5 mm/yr (2σ error) (Fig. 11A).

DISCUSSION

Interpretation of Hossack Station Incremental Slip Rate Data Set

The new Hossack Station fault slip rates demonstrate that the Hope fault is the fastest-slipping fault in the central Marlborough fault system, supporting earlier estimates of rapid slip (e.g., Freund, 1971; Van Dissen and Yeats, 1991; McMorran, 1991; Langridge et al., 2003; Khajavi et al., 2018). The Monte Carlo–modeled latest Pleistocene–Holocene Hope fault slip rate averaging offset E through to the present is 15.2 +1.1/–1.2 mm/yr, which is ~3× faster than the average latest Pleistocene–Holocene dextral slip rate of the Awatere fault, the next fastest–slipping fault in this section of the central Marlborough fault system (5.6 +0.4/–0.3 mm/yr documented at the Saxton River site; Zinke et al., 2017) (Figs. 11A, 11C). This rapid Hope fault slip rate reinforces the original inference of Van Dissen and Yeats (1991) that the Hope fault acts as the primary plate-boundary slip-transfer structure between the Alpine fault to the southwest (e.g., Berryman et al., 1992; Norris and Cooper, 2001; Sutherland et al., 2007; Langridge et al., 2010) and the fast-slipping Jordan-Kekerengu-Needles fault system to the northeast (Van Dissen and Yeats, 1991; Van Dissen et al., 2016; Kearse et al., 2017).

The new incremental rate data reveal a marked shift in slip rate along the Conway segment from older, slower latest Pleistocene to mid-Holocene average slip to younger, faster mid-Holocene to recent average slip. Specifically, offset C, dated at ca. 5.4 ka, separates two modes of behavior, where the incremental rate between ca. 5.4 and 13.8 ka is ~13 mm/yr (Figs. 11A, 11C). In contrast, the incremental rate averaged between offset C and the present (year 2019 CE) yields an average rate of ~19 mm/yr (Figs. 11A, 11C). The age of offset C itself (ca. 5.4 ka) does not hold any specific meaning and does not imply that a change in regional processes (e.g., tectonic loading) occurred at this time. Rather, it merely represents a point in time for which we were able to make a displacement-time measurement due to incision of channel C2 at that time. If the actual inflection point (i.e., the event that demarcated a shift in slip rate between fast and slow periods) occurred later in time (as in, closer to 13.8 ka than 5.4 ka), this change in slip rate from older and slower to younger and faster would be even more pronounced.

In addition to this variable slip-rate behavior of the Conway segment observed on the millennial time scale, there is much greater variability observed on the centennial time scale—by at least a factor of ~4, with incremental rates ranging from as slow 8 mm/yr (ca. 1.1 ka to present) to as fast as ~32 mm/yr (ca. 1.6–1.1 ka) (Figs. 11A, 11C). As noted above, the slowest incremental slip rate we measured is based on slip averaged from the time of stream incision at the beginning of offset A (ca. 1.1 ka) through to the present, including the current ongoing open interval following the most recent Conway segment surface rupture at ca. 1731–1840 CE (Hatem et al., 2019). As long as this open interval continues, this 8.2 +2.7/–1.5 mm/yr rate will progressively decrease. In other words, the OA slip rate can be considered a maximum rate until the next earthquake in the future, because this rate is sampled over a known incomplete interseismic cycle, meaning that the ~4× variability observed between the fastest and slowest incremental rates documented at the Hossack Station site is a minimum estimate of variability until the current interseismic cycle terminates at the next future surface-rupturing earthquake on the Conway segment (Fig. 11B).

Toward a Complete Dated Path of Earthquake Occurrence along the Conway Segment

Although we did not record a paleoearthquake chronology at the Hossack Station site, previous work by Hatem et al. (2019) determined the age ranges of the five most-recent events along the Conway segment at the Green Burn study site, ~40 km east of the Hossack Station site (pink star labeled GB on Fig. 1B; Fig. 11B). In that study, Hatem et al. (2019) showed that the five most-recent surface ruptures occurred since ca. 2 ka, with the age range of the fifth event back overlapping with age ranges of both offsets A and B at Hossack Station (Fig. 11B). As such, the youngest slip rate observed at the Hossack Station site potentially encompasses the five-event record observed at the Green Burn site. Alternatively, in light of the very long potential age range (ca. 1200 CE to 30 BCE) of the Hatem et al. (2019) Green Burn event 5, it is also possible that the fault slip that occurred in offset A accrued during the four most-recent events observed at the Green Burn site, because the age range of the fourth event back at Green Burn overlaps with the age range of offset A (Hatem et al., 2019).

Combining the Green Burn paleoseismic record with the dated offset A from the Hossack Station site, we can estimate the average slip per event along the Conway segment. Given that the Conway segment is a structural segment of the Hope fault, bounded on either end by a major structural complexity and without any other stepovers for >5 km along the length of the segment that might stop rupture propagation (e.g., Harris and Day, 1993; Wesnousky, 2008), it is plausible that the entire Conway segment ruptures along its full ~45 km length in large, surface-rupturing earthquakes. We

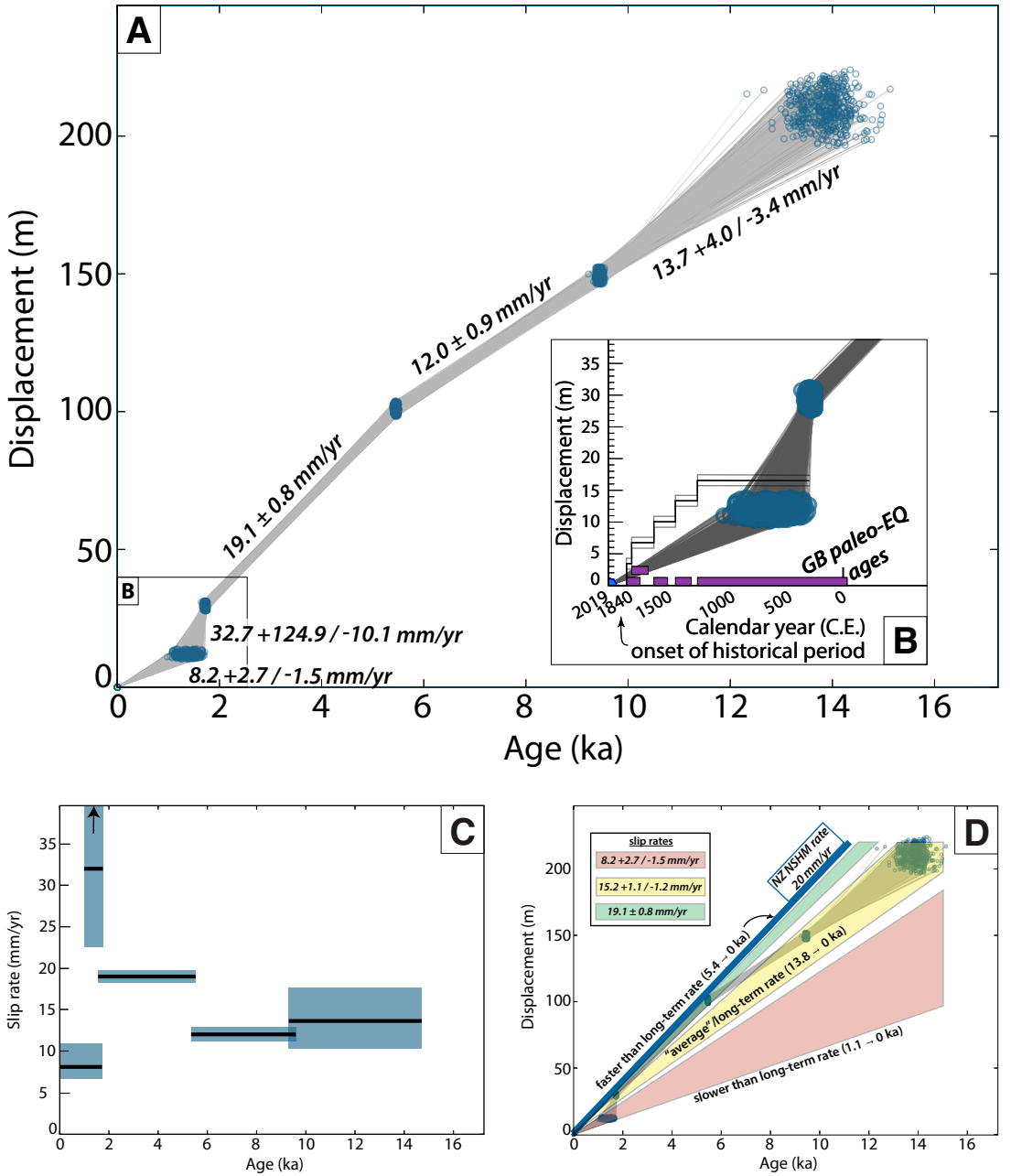

Figure 11. (A,B) Monte Carlo modeling of 10^6 iterations of displacement-time combinations between successive offset measurements on the Conway segment of the Hope fault. Each blue circle represents one displacement-time combination between offsets, and a thin gray line connects each blue circle. Modeling code is modified from Zinke et al. (2017, 2019). Panel A shows the full observed record at the Hossack Station site; inset figure (B) shows the youngest portion of the full record. In B, horizontal purple boxes represent paleoearthquake (paleo-EQ) ages determined by Hatem et al. (2019) at the Green Burn (GB) site (see purple star labeled GB on Fig. 1B). Black curve shows the single-event displacement estimates by Beauprêtre et al. (2012) at the Terako site (see green star labeled TK on Fig. 1B), with gray curves above and below denoting 2σ error on that estimate (~3.3 ± 1 m). (C) Incremental slip rates on the Conway segment of the Hope fault plotted against the time interval over which the rate is measured. Box height is the 2σ range, with preferred rate plotted as horizontal lines; box length is the age range of the slip rate. Note that the slip rate between offsets A and B plots off the scale, as indicated with the black arrow at the top of the box. (D) Modeled slip rates presented in panel A replotted with absolute slip-rate projections overlaid. Green projection shows offset C rate averaged through the origin, yellow projection shows offset E rate averaged through the origin, and red projection shows offset B rate averaged through the origin. Slip rate of 20 mm/yr assigned by the New Zealand National Seismic Hazard Model (NZ NSHM; Stirling et al., 2012) is shown as a solid blue line for reference.

therefore explore the possibility that cumulative offset measured at Hossack Station occurred in the same four to five events observed at Green Burn since 2 ka. With offset A measured at 12 ± 2 m (10–14 m, 2σ), and four or five earthquakes contributing slip to the offset A, we determine that average slip per event in the last ~1.1 k.y. along the Conway segment was 2.4 ± 0.4 m if all five paleoearthquakes happened after offset A, or 3.0 ± 0.5 m if only the past four paleo-earthquakes occurred after Offset A.

These estimates of single-event displacement are similar to estimates of single-event displacement derived from a combination of ground-penetrating radar and lidar analysis of geomorphic offsets at the Terako site, which lies nearly in the middle of the Conway segment (Beauprêtre et al., 2012) (green star labeled TK on Fig. 1B; Fig. 11B). There, single-event displacement is estimated to be 3.3 ± 1 m of slip averaged over the past 10 earthquakes.

Comparison of Hossack Station Record to Other Conway Segment Slip-Rate Estimates

The new incremental slip-rate record from the Hossack Station site facilitates comparisons with earlier estimates of slip rates on the Hope fault. The longest-term rate we document at the Hossack Station site indicates an average latest Pleistocene–Holocene slip since ca. 13.8 ka of 15.2 +1.1/–1.2 mm/yr. This average long-term slip rate is slower than previous estimates of the slip rate on the Conway segment of the Hope fault (McMorran, 1991 [18 ± 8 mm/yr]; Langridge et al., 2003 [≤23 ± 4 mm/yr; Van Dissen and Yeats, 1991 [28 ± 8 mm/yr]. All of these earlier rate estimates, however, were averaged over shorter, mid- to late Holocene time scales (McMorran, 1991 [ca. 2.6–3.6 ka, constrained by radiocarbon ages]; Langridge et al., 2003 [ca. 4.4 ka, constrained by radiocarbon ages]; Van Dissen and Yeats, 1991 [based on ca. 2.7 ka and 4.6 ka weathering rind age estimates of offset fluvial terraces]) and are most comparable to our well-constrained ~19 mm/yr offset C slip rate averaged over the past 5.4 k.y. These earlier, faster late Holocene rates are thus not in conflict with our slower, longer-term average slip rate of the Conway segment of the Hope fault. These comparisons reinforce our basic observation that slip rate along the Conway segment of the Hope fault was slower during latest Pleistocene–early Holocene time (~12–14 mm/yr) and faster during the mid- to late Holocene (~19 mm/yr).

Comparison of the Conway Segment Hossack Station Incremental Slip-Rate Record to the Late Holocene Hurunui–Hope River Incremental Slip-Rate Record

The new Hossack Station rates also facilitate comparisons with earlier estimates of incremental slip rate on the Hope fault. The only other incremental slip-rate record available for the Hope fault comes from Khajavi et al. (2018), who combined previously measured offsets from Cowan (1990), Cowan and McGlone (1991), and Langridge and Berryman (2005), as well as small offsets measured from lidar data novel to their study, with geochronologic constraints from these previous studies and a nearby paleoseismologic study (Khajavi et al., 2016) to document late Holocene slip-rate changes during the past ~2.3 k.y. Specifically, Khajavi et al. (2018) used the paleoearthquake timing of Khajavi et al. (2016) combined with a compilation of their small-offset measurements from the Hope River–Hurunui section of the fault to determine earthquake-by-earthquake incremental slip for the past 1.6 k.y. In addition, they compared the rates derived from these individual earthquake offsets with a ca. 2.3 ka rate based on cumulative fault displacements and surface ages measured at three sites along the Hurunui segment (Cowan, 1990; Cowan and McGlone, 1991; Langridge and Berryman, 2005).

Based on these data, Khajavi et al. (2018) reported a fast average rate of 25 +3.4/–3.2 mm/yr between ca. 1.6 and 2.3 ka. The cumulative slip constraint used on the young end of this interval overlaps with two closely spaced paleoearthquakes identified by Khajavi et al. (2016) at ca. 1.5 and 1.6 ka; these two events were followed by four younger earthquakes. Using the data presented by Khajavi et al. (2018), and assuming that their fifth and sixth earthquakes back mark the end of a previous fast period extending back to at least 2.3 ka, there is a marked inflection point in the rate of coseismic strain release along the Hurunui–Hope River segments of the Hope fault at ca. 1.5 ka. Prior to 1.5 ka, the Khajavi et al. (2018) data set suggests a slip rate of ~30 mm/yr encompassing ~26 m of slip between 1.5 ka and 2.3 ka, which was followed by a much slower rate of ~6 mm/yr based on ~8 m of slip occurring during the four youngest events, including the historic 1888 C.E. Amuri rupture.

Although the time spans of the incremental rates we measured at the Hossack Station site do not exactly match those discussed by Khajavi et al. (2018), both studies reveal a similar pattern of relatively slow slip rate during the latest Holocene (since 1.5 ka along the Hurunui–Hope River segments and since 1.1 ka at the Hossack Station site on the Conway segment) that was preceded by a period of faster slip (extending from 1.5 ka to as least 2.3 ka along the Hurunui–Hope River segments, versus a very fast interval between 1.1 and 1.6 ka and a fast but slightly slower incremental rate between 1.6 ka and 5.4 ka at the Hossack Station site). Thus, patterns of incremental slip-rate variability along the Hope fault appear to be relatively consistent across the major structural discontinuity of the Hanmer pull-apart basin over time scales that span multiple earthquakes and tens of meters of slip.

Although the relative pattern of incremental slip-rate variability may be consistent across the Hanmer Basin, the absolute measurements of cumulative slip along the Hurunui–Hope River segments are about a factor of two less than those observed in our study along the Conway segment. This is illustrated by the 1.6 ka offset estimates that are common to both studies. Specifically, Khajavi et al. (2018) reported ~15 m of fault slip since ca. 1.6 ka on the Hurunui–Hope River segments of the Hope fault, compared to our preferred slip estimate of 29 m since 1.6 ka (offset B) at the Hossack Station site. Much of this difference is likely due to the fact that the Hope fault is double stranded in the area of the Khajavi et al. (2018) measurements; the more southerly Kakapo strand of the Hope fault extends westward for a distance of ~40 km subparallel to the northern strand segments from the Kakapo fault–Hope River strand

intersection at Glynne Wye (Fig. 1B). Thus, the Khajavi et al. (2018) rates do not span the entire width of the Hope fault zone. Assuming that there is no difference in temporal strain accumulation patterns along the Hope fault on either side of the Hanmer Basin, the apparent consistency in rate variability relative to the mismatch in cumulative displacement between the single-stranded Conway segment and the northern Hurunui–Hope Shelter strand of the double-stranded Hope fault to the west suggests that the difference in total dextral slip may be taken up by slip that is partitioned onto the southern, Kakapo segment of the Hope fault system. If correct, this would suggest that the slip rate of the Kakapo strand may be somewhat faster than previous estimates of 4.4–8.4 mm/yr averaged over the past ~5.3 k.y. (Knuepfer, 1988, 1992) and 4.7–8.0 mm/yr averaged since ca. 17 ± 2 ka (Cowan et al., 1989), at least during late Holocene time.

The broadly synchronous along-strike changes in late Holocene incremental rate along the Conway and Hope River–Hurunui segments suggest coordinated waxing and waning of slip rate along the entire Hope fault. Although this behavior would not be surprising for single earthquake sequences, which indeed likely occurs along the Hope fault (Hatem et al., 2019), these accelerations and decelerations in Hope fault slip span multiple earthquakes and tens of meters of fault slip. This observation indicates that whatever controls this nonconstant slip rate behavior must operate over time spans longer than single earthquake cycles. The exact mechanisms that control such behavior remain incompletely understood, but could be related to changes in the strength of the fault through time (e.g., Dolan et al., 2007, 2016; Oskin et al., 2008; Zinke et al., 2017, 2019) and/or changes in the rate of elastic strain accumulation, which in turn could be controlled by either system-level tradeoffs among mechanically complementary faults within complex plate-boundary fault systems (e.g., Dolan et al., 2016; Wedmore et al., 2017) or changes in relative plate motion rates (e.g., Anderson, 1975; Pollitz, 1986; Romanowicz, 1993; Dolan et al., 2016; Meade and Loveless, 2017). Whatever the exact cause of the variable incremental slip rate on the Hope fault, the new Hossack Station data add to a growing body of evidence that such slip-rate variations may be more common than previously thought along some faults (e.g., Wallace, 1987; Friedrich et al., 2003; Weldon et al., 2004; Dolan et al., 2007, 2016; Sieh et al., 2008; Gold and Cowgill, 2011; Goldfinger et al., 2013; Ninis et al., 2013; Onderdonk et al., 2015; Zinke et al., 2017, 2019; Khajavi et al., 2018). Future documentation of additional detailed, well-dated incremental slip-rate records from many more faults will provide constraints on the variability (or constancy) of fault slip rates that will, in turn, facilitate a more thorough understanding of the mechanical controls on spatial-temporal patterns of fault slip.

Implications for Probabilistic Seismic Hazard Modeling

Geologic slip rate is one of the most basic inputs for probabilistic seismic hazard analysis codes (e.g., Stirling et al., 2012; Dawson and Weldon, 2013; Field et al., 2013; Petersen et al., 2015). Typically, a multi-millennial average slip rate is preferred, because such a rate is thought to capture the overall behavior of a fault. However, the variability of incremental slip rates presented in this manuscript highlights the conundrum currently facing modeling decisions when slip rates must be selected as inputs for deformation models. For instance, with the Hossack Station data set, selecting the long-term (ca. 13.8 ka rate averaged through present day) underestimates the 5.4 ka average rate, which is another multi-millennial, "long-term" rate (Fig. 11D). Additionally, as previously discussed, both of these multi-millennial rates (slip rates BC and CD) are slower than the centennial rate AB (Fig. 11D).

The slip rate for the Conway segment of the Hope fault as currently used in the 2010 New Zealand National Seismic Hazard Model (fault segment 403) is 20 mm/yr (Stirling et al., 2012). This rate is based on a combination of a mid-Holocene slip rate (Langridge et al., 2003) and a rate based on potentially unreliable weathering-rind age control (Knuepfer, 1992). The well-dated, longer-term (latest Pleistocene–Holocene) Conway segment slip rate of ~15 mm/yr (yellow swath on Fig. 11D) that we document in this paper is slower than the currently utilized value by ~25%. As noted above, although the longer-term rate we measure is less than the currently used value for slip rate along the Conway segment, the Hossack Station mid- to late Holocene slip rate BC (green swath on Fig. 11D, spanning 1.6 ka to 5.4 ka) is a closer match to the 20 mm/yr rate utilized in the New Zealand National Seismic Hazard Model. The fastest rate recorded at Hossack Station (rate AB of ~32 mm/yr) far exceeds the rate used for probabilistic seismic hazard analyses.

Which slip rate (short-term, long-term, or a combination) best represents how a fault is behaving at present day and how it will continue to behave within the near future remains an open question. As deformation models and probabilistic seismic hazard codes advance to allow the use of higher-resolution geologic input data, variability in incremental slip rates, such as that documented herein along the Hope fault at the Hossack Station site as well as other sites along the Hope fault (e.g., Khajavi et al., 2018), may be utilized to determine time-dependent hazard within regional plate-boundary fault systems (Hatem et al., 2020; Van Dissen et al., 2020).

CONCLUSIONS

New incremental rate data demonstrate that the slip rate of the Conway segment of the Hope fault, the main plate-boundary strike-slip fault in this area of the South Island of the Pacific-Australia plate boundary, has varied significantly during Holocene–latest Pleistocene time. These incremental slip rates range from a latest Holocene (1.1 ka–present) rate of 8.2 +2.7/–1.5 mm/yr, to a rate of 32.7 +124.9/–10.1 mm/yr averaged over 1.6–1.1 ka, to 19.1 ± 0.8 mm/yr between 5.4 and 1.6 ka, to 12.0 ± 0.9 mm/yr between 9.4 and 5.4 ka, to 13.7 +4.0/–3.4 mm/yr from 13.8 to 9.4 ka. We observe a variation by a factor of ~1.5–4× times within this slip-rate data set, similar to other faults in the Marlborough fault system as observed in incremental slip-rate records measured using cumulative slip measurements along the Awatere (Zinke et al., 2017) and Clarence (Zinke et al., 2019) faults. These

data add to a growing body of evidence that slip rate on some faults varies considerably over displacement scales of tens to hundreds of meters, and may vary in complex patterns across Hope fault segments, as shown in a comparison of our record of incremental slip rates to previous slip rate estimates for farther west along the Hurunui–Hope River segments (Khajavi et al., 2018). Furthermore, our results, when combined with slip-rate estimates from Khajavi et al. (2018), suggest the potential recent (ca. 1.6 ka) importance of the Kakapo fault in strain partitioning within the Hope fault system.

Not only are such variations in geologic slip rate of critical importance for understanding the mechanics and earthquake behavior of major fault systems, they are also of great importance in probabilistic seismic hazard analysis, in which fault slip rate represents a primary model input. Variable slip rates such as those that we document for the Hope fault are not currently represented in probabilistic seismic hazard analyses due to the current configuration of deformation and hazard modeling codes. Incorporation of variable rates into probabilistic hazard assessments is, however, a current direction in probabilistic seismic hazard research (e.g., Zeng, 2018; Hatem et al., 2020; Van Dissen et al., 2020). The Hossack Station record highlights the necessity of understanding the incremental displacement history (i.e., the dated path) of major faults in order to more fully understand how plate-boundary fault systems accommodate relative plate motion in time and space.

ACKNOWLEDGMENTS

Funded by U.S. National Science Foundation grants EAR-1321914 (Dolan) and EAR-1321912 (Rhodes), with additional funding and field support from GNS Science. We thank John Angland (Red Stag Ltd.) and Mel and Baldrick Jones (Hossack Station) for permission to conduct this study on their property. We thank Genevieve Coffey and Colin Chupik for field assistance. We also thank reviewers Tim Little and Mark Quigley for thought-provoking and helpful reviews, as well as Associate Editor Andrew Zuza for swift and careful handling of our manuscript.

REFERENCES CITED

Anderson, D.L., 1975, Accelerated plate tectonics: Science, v. 187, p. 1077–1079, https://doi.org/10.1126/science.187.4181.1077.

Beauprêtre, S., Garambois, S., Manighetti, I., Malavieille, J., Sénéchal, G., Chatton, M., Davies, T., Larroque, C., Rousset, D., Cotte, N., and Romano, C., 2012, Finding the buried record of past earthquakes with GPR-based paleoseismology: A case study on the Hope fault, New Zealand: Geophysical Journal International, v. 189, p. 73–100, https://doi.org/10.1111/j.1365-246X.2012.05366.x.

Berryman, K.R., Beanland, S., Cooper, A., Cutten, H.N., and Norris, R.J., 1992, The Alpine Fault, New Zealand: Variation in Quaternary structural style and geomorphic expression: Annales Tectonicae, v. VI, p. 126–163.

Bronk Ramsey, C., 2009, Bayesian analysis of radiocarbon dates: Radiocarbon, v. 51, p. 337–360, https://doi.org/10.1017/S0033822200033865.

Bull, W.B., 1991, Geomorphic Response to Climatic Change: New York, Blackburn Press, 352 p.

Bull, W.B., 2008, Tectonic Geomorphology of Mountains: A New Approach to Paleoseismology: Malden, Massachusetts, John Wiley & Sons, 328 p.

Bull, W.B., and Knuepfer, P.L.K., 1987, Adjustments by the Charwell River, New Zealand, to uplift and climatic changes: Geomorphology, v. 1, p. 15–32, https://doi.org/10.1016/0169-555X(87)90004-3.

Cowan, H.A., 1990, Late Quaternary displacements on the Hope fault at Glynn Wye, North Canterbury: New Zealand Journal of Geology and Geophysics, v. 32, p. 285–293, https://doi.org/10.1080/00288306.1990.10425686.

Cowan, H.A., 1991, The North Canterbury earthquake of September 1, 1888: Journal of the Royal Society of New Zealand, v. 21, p. 1–12, https://doi.org/10.1080/03036758.1991.10416105.

Cowan, H.A., and McGlone, M.S., 1991, Late Holocene displacements and characteristic earthquakes on the Hope River segment of the Hope fault, New Zealand: Journal of the Royal Society of New Zealand, v. 21, p. 373–384, https://doi.org/10.1080/03036758.1991.10420834.

Cowan, H.A., Pettinga, J.R., and Smith, I.E.M., 1989, Transtension and structural complexity along the Hope Fault: Glynn Wye to Hammer Basin, North Canterbury: Geological Society of New Zealand Miscellaneous Publication 43, 31 p.

Dawson, T.E., and Weldon, R.J., II, 2013, Appendix B: Geologic-slip-rate data and geologic deformation model, *in* Field, E.H., Biasi, G.P., Bird, P., Dawson, T.E., Felzer, K.R., Jackson, D.D., Johnson, K.M., Jordan, T.H., Madden, C., Michael, A.J., Milner, K.R., Page, M.T., Parsons, T., Powers, P.M., Shaw, B.E., Thatcher, W.R., Weldon, R.J., II, and Zeng, Y., Uniform California Earthquake Rupture Forecast, Version 3 (UCERF3)—The Time-Independent Model: U.S. Geological Survey Open-File Report 2013-1165, California Geological Survey Special Report 228, and Southern California Earthquake Center Publication 1792, 29 p., http://pubs.usgs.gov/of/2013/1165/.

DeMets, C., Gordon, R.G., and Argus, D.F., 2010, Geologically current plate motions: Geophysical Journal International, v. 181, p. 1–80, https://doi.org/10.1111/j.1365-246X.2009.04491.x.

Dolan, J.F., Bowman, D.D., and Sammis, C.G., 2007, Long-range and long-term fault interactions in Southern California: Geology, v. 35, p. 855–858, https://doi.org/10.1130/G23789A.1.

Dolan, J.F., McAuliffe, L.J., Rhodes, E.J., McGill, S.F., and Zinke, R., 2016, Extreme multi-millennial slip rate variations on the Garlock fault, California: Strain super-cycles, potentially time-variable fault strength, and implications for system-level earthquake occurrence: Earth and Planetary Science Letters, v. 446, p. 123–136, https://doi.org/10.1016/j.epsl.2016.04.011.

Field, E.H., Biasi, G.P., Bird, P., Dawson, T.E., Felzer, K.R., Jackson, D.D., Johnson, K.M., Jordan, T.H., Madden, C., Michael, A.J., Milner, K.R., Page, M.T., Parsons, T., Powers, P.M., Shaw, B.E., Thatcher, W.R., Weldon, R.J., II, and Zeng, Y., 2013, Uniform California Earthquake Rupture Forecast, Version 3 (UCERF3)—The Time-Independent Model: U.S. Geological Survey Open-File Report 2013-1165, California Geological Survey Special Report 228, and Southern California Earthquake Center Publication 1792, 97 p., http://pubs.usgs.gov/of/2013/1165/.

Freund, R., 1971, The Hope fault: A strike slip fault in New Zealand: New Zealand Geological Survey Bulletin 86, 49 p.

Friedrich, A.M., Wernicke, B.P., Niemi, N.A., Bennett, R.A., and Davis, J.L., 2003, Comparison of geodetic and geologic data from the Wasatch region, Utah, and implications for the spectral character of Earth deformation at periods of 10 to 10 million years: Journal of Geophysical Research, v. 108, 2199, https://doi.org/10.1029/2001JB000682.

Gold, R.D., and Cowgill, E., 2011, Deriving fault-slip histories to test for secular variation in slip, with examples from the Kunlun and Awatere faults: Earth and Planetary Science Letters, v. 301, p. 52–64, https://doi.org/10.1016/j.epsl.2010.10.011.

Goldfinger, C., Ikeda, Y., Yeats, R.S., and Ren, J., 2013, Superquakes and supercycles: Seismological Research Letters, v. 84, p. 24–32, https://doi.org/10.1785/0220110135.

Harris, R.A., and Day, S.M., 1993, Dynamics of fault interaction: Parallel strike-slip faults: Journal of Geophysical Research, v. 98, p. 4461–4472, https://doi.org/10.1029/92JB02272.

Hatem, A.E., Dolan, J.F., Zinke, R.W., Van Dissen, R.J., McGuire, C.P., and Rhodes, E.J., 2019, A 2000 yr paleoearthquake record along the Conway segment of the Hope fault: Implications for patterns of earthquake occurrence in northern South Island and southern North Island, New Zealand: Bulletin of the Seismological Society of America, v. 109, p. 2216–2239, https://doi.org/10.1785/0120180313.

Hatem, A.E., Gold, R.D., Briggs, R.W., Field, E.H., Powers, P.M., Collett, C.M., and Delano, J.E., 2020, Development of a Fault Source Parameters Database and Updates of the Fault Source Model for the US National Seismic Hazard Model: Seismological Research Letters, v. 91, p. 1240, https://doi.org/10.1785/0220200043.

Hogg, A.G., Hua, Q., Blackwell, P.G., Niu, M., Buck, C.E., Guilderson, T.P., Heaton, T.J., Palmer, J.G., Reimer, P.J., Reimer, R.W., Turney, C.S.M., and Zimmerman, S.R.H., 2013, SHCal13 Southern Hemisphere calibration, 0–50,000 years cal BP: Radiocarbon, v. 55, p. 1889–1903, https://doi.org/10.2458/azu_js_rc.55.16783.

Kearse, J., Little, T.A., Van Dissen, R.J., Barnes, P.M., Langridge, R., Mountjoy, J., Ries, W., Villamor, P., Clark, K.J., Benson, A., Lamarche, G., Hill, M., and Hemphill-Haley, M., 2017, Onshore to offshore ground-surface and seabed rupture of the Jordan–Kekerengu–Needles fault network during the 2016 M_w 7.8 Kaikōura earthquake, New Zealand: Bulletin of the Seismological Society of America, v. 108, p. 1573–1595, https://doi.org/10.1785/0120170304.

Khajavi, N., Langridge, R.M., Quigley, M.C., Smart, C., Rezanejad, A., and Martín-González, F., 2016, Late Holocene rupture behavior and earthquake chronology on the Hope fault,

New Zealand: Geological Society of America Bulletin, v. 128, p. 1736–1761, https://doi.org/10.1130/B31199.1.

Khajavi, N., Nicol, A., Quigley, M.C., and Langridge, R.M., 2018, Temporal slip-rate stability and variations on the Hope Fault, New Zealand, during the late Quaternary: Tectonophysics, v. 738, p. 112–123, https://doi.org/10.1016/j.tecto.2018.05.001.

Knuepfer, P.L.K., 1988, Estimating ages of late Quaternary stream terraces from analysis of weathering rinds and soils: Geological Society of America Bulletin, v. 100, p. 1224–1236, https://doi.org/10.1130/0016-7606(1988)100<1224:EAOLQS>2.3.CO;2.

Knuepfer, P.L.K., 1992, Temporal variations in latest Quaternary slip across the Australian-Pacific plate boundary, northeastern South Island, New Zealand: Tectonics, v. 11, p. 449–464, https://doi.org/10.1029/91TC02890.

Kozaci, Ö., Dolan, J., Finkel, R., and Hartleb, R., 2007, Late Holocene slip rate for the North Anatolian fault, Turkey, from cosmogenic ^{36}Cl geochronology: Implications for the constancy of fault loading and strain release rates: Geology, v. 35, p. 867–870, https://doi.org/10.1130/G23187A.1.

Langridge, R.M., and Berryman, K.R., 2005, Morphology and slip rate of the Hurunui section of the Hope fault, South Island, New Zealand: New Zealand Journal of Geology and Geophysics., v. 48, p. 43–57, https://doi.org/10.1080/00288306.2005.9515097.

Langridge, R., Campbell, J., Hill, N., Pere, V., Pope, J., Pettinga, J., Estrada, B., and Berryman, K., 2003, Paleoseismology and slip rate of the Conway Segment of the Hope Fault at Greenburn Stream, South Island, New Zealand: Annals of Geophysics, v. 46, p. 1119–1140, https://doi.org/10.4401/ag-3449.

Langridge, R.M., Villamor, P., Basili, R., Almond, P., Martinez-Diaz, J.J., and Canora, C., 2010, Revised slip rates for the Alpine fault at Inchbonnie: Implications for plate boundary kinematics of South Island, New Zealand: Lithosphere, v. 2, p. 139–152, https://doi.org/10.1130/L88.1.

Langridge, R.M., Ries, W.F., Litchfield, N.J., Villamor, P., Van Dissen, R.J., Barrell, D.J.A., Rattenbury, M.S., Heron, D.W., Haubrock, S., Townsend, D.B., Lee, J.M., Berryman, K.R., Nicol, A., Cox, S.C., and Stirling, M.W., 2016, The New Zealand Active Faults Database: New Zealand Journal of Geology and Geophysics, v. 59, p. 86–96, https://doi.org/10.1080/00288306.2015.1112818.

Lensen, G.J., 1968, Analysis of progressive fault displacement during downcutting at the Branch River terraces, South Island, New Zealand: Geological Society of America Bulletin, v. 79, p. 545–556, https://doi.org/10.1130/0016-7606(1968)79[545:AOPFDD]2.0.CO;2.

Lewis, C.J., Sancho, C., McDonald, E.V., Peña-Monné, J.L., Puevo, E.L., Rhodes, E.J., Calle, M., and Soto, R., 2017, Post-tectonic landscape evolution in NE Iberia using a staircase of terraces: Combined effects of uplift and climate: Geomorphology, v. 292, p. 85–103, https://doi.org/10.1016/j.geomorph.2017.04.037.

Litchfield, N.J., Van Dissen, R., Sutherland, R., Barnes, P.M., Cox, S.C., Norris, R., Beavan, R.J., Langridge, R., Villamor, P., Berryman, K., Stirling, M., Nicol, A., Nodder, S., Lamarche, G., Barrell, D.J.A., Pettinga, J.R., Little, T., Pondard, N., Mountjoy, J.J., and Clark, K., 2014, A model of active faulting in New Zealand: New Zealand Journal of Geology and Geophysics, v. 57, p. 32–56, https://doi.org/10.1080/00288306.2013.854256.

Litchfield, N.J., Villamor, P., Van Dissen, R.J., Nicol, A., Barnes, P.M., Barrell, D.J.A., Pettinga, J.R., Langridge, R.M., Little, T.A., Mountjoy, J.J., Ries, W.F., Rowland, J., Fenton, C., Stirling, M.W., Kearse, J., Berryman, K.R., Cochran, U.A., Clark, K.J., Hemphill-Haley, M., Khajavi, N., Jones, K.E., Archibald, G., Upton, P., Asher, C., Benson, A., Cox, S.C., Gasston, C., Hale, D., Hall, B., Hatem, A.E., Heron, D.W., Howarth, J., Kane, T.J., Lamarche, G., Lawson, S., Lukovic, B., McColl, S.T., Madugo, C., Manousakis, J., Noble, D., Pedley, K., Sauer, K., Stahl, T., Strong, D.T., Townsend, D.B., Toy, V., Williams, J., Woelz, S., and Zinke, R., 2018, Surface rupture of multiple crustal faults in the M_w 7.8 2016 Kaikōura earthquake, New Zealand: Bulletin of the Seismological Society of America, v. 108, p. 1496–1520, https://doi.org/10.1785/0120170300.

Mason, D.P.M., Little, T.A., and Van Dissen, R.J., 2006, Refinements to the paleoseismic chronology of the eastern Awatere fault from trenches near Upcot Saddle, Marlborough, New Zealand: New Zealand Journal of Geology and Geophysics, v. 49, p. 383–397, https://doi.org/10.1080/00288306.2006.9515175.

McKay, A., 1890, On the earthquakes of September, 1888, in the Amuri and Marlborough districts of the South Island: New Zealand Geological Survey Reports of Geological Explorations, v. 20, p. 1–16.

McMorran, T.J., 1991, The Hope Fault at Hossack Station east of Hanmer Basin, North Canterbury [M.S. thesis]: Christchurch, New Zealand, University of Canterbury, 81 p.

Meade, B.J., and Loveless, J.P., 2017, Block motion changes in Japan triggered by the 2011 Great Tohoku earthquake: Geochemistry Geophysics Geosystems, v. 18, p. 2459–2466, https://doi.org/10.1002/2017GC006983.

Ninis, D., Little, T.A., Van Dissen, R.J., Litchfield, N.J., Smith, E.G.C., Wang, N., Rieser, U., and Henderson, C.M., 2013, Slip rate on the Wellington fault, New Zealand, during the late Quaternary: Evidence for variable slip during the Holocene: Bulletin of the Seismological Society of America, v. 103, p. 559–579, https://doi.org/10.1785/0120120162.

Noriega, G.R., Arrowsmith, J.R., Grant, L.B., and Young, J.J., 2006, Stream channel offset and late Holocene slip rate of the San Andreas fault at the Van Matre Ranch site, Carrizo Plain, California: Bulletin of the Seismological Society of America, v. 96, p. 33–47, https://doi.org/10.1785/0120050094.

Norris, R.J., and Cooper, A.F., 2001, Late Quaternary slip rates and slip partitioning on the Alpine Fault, New Zealand: Journal of Structural Geology, v. 23, p. 507–520.

Onderdonk, N.W., McGill, S.F., and Rockwell, T.K., 2015, Short-term variations in slip rate and size of prehistoric earthquakes during the past 2000 years on the northern San Jacinto fault zone, a major plate-boundary structure in southern California: Lithosphere, v. 7, p. 211–234, https://doi.org/10.1130/L393.1.

Oskin, M., Perg, L., Shelef, E., Strane, M., Gurney, E., Singer, B., and Zhang, X., 2008, Elevated shear zone loading rate during an earthquake cluster in eastern California: Geology, v. 36, p. 507–510, https://doi.org/10.1130/G24814A.1.

Petersen, M.D., Moschetti, M.P., Powers, P.M., Mueller, C.S., Haller, K.M., Frankel, A.D., Zeng, Y., Rezaeian, S., Harmsen, S.C., Boyd, O.S., Field, N., Chen, R., Rukstales, K.S., Luco, N., Wheeler, R.L., Williams, R.A., and Olsen, A.H., 2015, The 2014 United States National Seismic Hazard Model: Earthquake Spectra, v. 31, p. S1–S30, https://doi.org/10.1193/120814EQS210M.

Pollitz, F.F., 1986, Pliocene change in Pacific-plate motion: Nature, v. 320, p. 738–741, https://doi.org/10.1038/320738a0.

Rhodes, E.J., 2015, Dating sediments using potassium feldspar single-grain IRSL: Initial methodological considerations: Quaternary International, v. 362, p. 14–22, https://doi.org/10.1016/j.quaint.2014.12.012.

Romanowicz, B., 1993, Spatiotemporal patterns in the energy release of great earthquakes: Science, v. 260, p. 1923–1926, https://doi.org/10.1126/science.260.5116.1923.

Salisbury, J.B., Arrowsmith, J.R., Brown, N., Rockwell, T., Akçiz, S., and Ludwig, L.G., 2018, The age and origin of small offsets at Van Matre Ranch along the San Andreas fault in the Carrizo Plain, California: Bulletin of the Seismological Society of America, v. 108, p. 639–653, https://doi.org/10.1785/0120170162.

Sieh, K., Natawidjaja, D.H., Meltzner, A.J., Shen, C.-C., Cheng, H., Li, K-S., Suwargadi, B.W., Galetzka, J., Philibosian, B., and Edwards, R.L., 2008, Earthquake supercycles inferred from sea-level changes recorded in the corals of west Sumatra: Science, v. 322, p. 1674–1678, https://doi.org/10.1126/science.1163589.

Stirling, M., McVerry, G., Gerstenberger, M., Litchfield, N., Van Dissen, R., Berryman, K., Barnes, P., Wallace, L., Villamor, P., Langridge, R., Lamarche, G., Nodder, S., Reyners, M., Bradley, B., Rhoades, D., Smith, W., Nicol, A., Pettinga, J., Clark, K., and Jacobs, K., 2012, National Seismic Hazard Model for New Zealand: 2010 update: Bulletin of the Seismological Society of America, v. 102, p. 1514–1542, https://doi.org/10.1785/0120110170.

Sutherland, R., Eberhart-Phillips, D., Harris, R.A., Stern, T., Beavan, J., Ellis, S., Henrys, S., Cox, S., Norris, R.J., Berryman, K.R., Townend, J., Bannister, S., Pettinga, J., Leitner, B., Wallace, L., Little, T.A., Cooper, A.F., Yetton, M., and Stirling, M., 2007, Do great earthquakes occur on the Alpine fault in central South Island, New Zealand?, *in* Okaya, D., Stern, T., and Davey, F., eds., A Continental Plate Boundary: Tectonics at South Island, New Zealand: American Geophysical Union Geophysical Monograph 175, https://doi.org/10.1029/175GM12.

Van Der Woerd, J., Tapponnier, P., Ryerson, F.J., Meriaux, A.-S., Meyer, B., Gaudemer, Y., Finkel, R.C., Caffee, M.W., Zhao, G., and Xu, Z., 2002, Uniform postglacial slip-rate along the central 600 km of the Kunlun Fault (Tibet), from ^{26}Al, ^{10}Be, and ^{14}C dating of riser offsets, and climatic origin of the regional morphology: Geophysical Journal International, v. 148, p. 356–388, https://doi.org/10.1046/j.1365-246x.2002.01556.x.

Van Dissen, R., and Yeats, R.S., 1991, Hope fault, Jordan thrust, and uplift of the Seaward Kaikoura Range, New Zealand: Geology, v. 19, p. 393–396, https://doi.org/10.1130/0091-7613(1991)019<0393:HFJTAU>2.3.CO;2.

Van Dissen, R.J., Little, T.A., Burke, R.M., Tonkin, P.J., Norton, K.P., Bacon, S.N., Bowers, R., Goldstein, H.L., Redwine, J.R., Sutherland, D.G., Tillinghast, S.F., Kearse, J.R., Whattam, J., Townsend, D.B., Benson, A.M., Hill, M.P., Ashraf, S., and Wang, N., 2016, Late Quaternary dextral slip rate of the Kekerengu fault: New Zealand's third fastest on-land fault, *in* Riesselman, C., and Roben, A., eds., Abstracts, GeoSciences 2016, Wanaka: Geoscience Society of New Zealand Miscellaneous Publication 142A, p. 89.

Van Dissen, R., Abbott, E., Zinke, R., Ninis, D., Dolan, J.F., Little, T.A., Rhodes, E.J., Litchfield, N.J., and Hatem, A.E., 2020,

Slip rate variations on major strike-slip faults in central New Zealand and potential impacts on hazard estimation: Paper 6 presented at New Zealand Society for Earthquake Engineering Annual Conference, Wellington, 22–24 April.

Wallace, L.M., Barnes, P., Beavan, J., Van Dissen, R., Litchfield, N., Mountjoy, J., Langridge, R., Lamarche, G., and Pondard, N., 2012, The kinematics of a transition from subduction to strike-slip: An example from the central New Zealand plate boundary: Journal of Geophysical Research, v. 117, B02405, https://doi.org/10.1029/2011JB008640.

Wallace, R.E., 1987, Grouping and migration of surface faulting and variations in slip rates on faults in the Great Basin province: Bulletin of the Seismological Society of America, v. 77, p. 868–876.

Wedmore, L.N.J., Walker, J.F., Roberts, G.P., Sammonds, P.R., McCaffrey, K.J.W., and Cowie, P.A., 2017, A 667 year record of coseismic and interseismic Coulomb stress changes in central Italy reveals the role of fault interaction in controlling irregular earthquake recurrence intervals: Journal of Geophysical Research: Solid Earth, v. 122, p. 5691–5711, https://doi.org/10.1002/2017JB014054.

Weldon, R.J., II, and Sieh, K.E., 1985, Holocene rate of slip and tentative recurrence interval for large earthquakes of the San Andreas fault, Cajon Pass, southern California: Geological Society of America Bulletin, v. 96, p. 793–812, https://doi.org/10.1130/0016-7606(1985)96<793:HROSAT>2.0.CO;2.

Weldon, R., Scharer, K., Fumal, T., and Biasi, G., 2004, Wrightwood and the earthquake cycle: What a long recurrence record tells us about how faults work: GSA Today, v. 14, no. 9, p. 4–10, https://doi.org/10.1130/1052-5173(2004)014<4:WATECW>2.0.CO;2.

Wesnousky, S.G., 2008, Displacement and geometrical characteristics of earthquake surface ruptures: Issues and implications for seismic-hazard analysis and the process of earthquake rupture: Bulletin of the Seismological Society of America, v. 98, p. 1609–1632, https://doi.org/10.1785/0120070111.

Wood, R.A., Pettinga, J.R., Bannister, S., Lamarche, G., and McMorran, T.J., 1994, Structure of the Hanmer strike-slip basin, Hope fault, New Zealand: Geological Society of America Bulletin, v. 106, p. 1459–1473, https://doi.org/10.1130/0016-7606(1994)106<1459:SOTHSS>2.3.CO;2.

Zeng, Y., 2018, Analysis of mean seismic ground motion and its uncertainty based on the UCERF3 geologic slip-rate uncertainty for California: Seismological Research Letters, v. 89, p. 1410–1419, https://doi.org/10.1785/0220170114.

Zinke, R., Dolan, J.F., Rhodes, E.J., Van Dissen, R., and McGuire, C.P., 2017, Highly variable latest Pleistocene–Holocene incremental slip rates on the Awatere fault at Saxton River, South Island, New Zealand, revealed by lidar mapping and luminescence dating: Geophysical Research Letters, v. 44, p. 11,301–11,310, https://doi.org/10.1002/2017GL075048.

Zinke, R., Dolan, J.F., Rhodes, E.J., Van Dissen, R., McGuire, C.P., Hatem, A.E., Brown, N.D., and Langridge, R.M., 2019, Multi-millennial incremental slip rate variability of the Clarence fault at the Tophouse Road site, Marlborough fault system, New Zealand: Geophysical Research Letters, v. 46, p. 717–725, https://doi.org/10.1029/2018GL080688.